Ice accretion in cryogenic heat exchangers

Dimensioning, building, testing and validating a heat exchanger rig for freezing condensate for various future aircraft engine applications

Degree project report in Mobility engineering

OLIVER KADI

DEPARTMENT OF MECHANICS AND MARITIME SCIENCES
CHALMERS UNIVERSITY OF TECHNOLOGY
Gothenburg, Sweden 2024
www.chalmers.se

DEGREE PROJECT REPORT 2024

Ice accretion in cryogenic heat exchangers

Dimensioning, building, testing and validating a heat exchanger rig for freezing condensate for various future aircraft engine applications

OLIVER KADI

Department of Mechanics and Maritime Sciences
CHALMERS UNIVERSITY OF TECHNOLOGY
Gothenburg, Sweden 2024

Ice accretion in cryogenic heat exchangers
Dimensioning, building, testing and validating a heat exchanger rig for freezing condensate for various future aircraft engine applications
OLIVER KADI

Co-Supervisor: Petter Miltén, Department of Mechanics and Maritime Sciences
Co-Supervisor: Isak Jonsson, Department of Mechanics and Maritime Sciences
Company Supervisor: Anders Lundbladh, GKN Aerospace
Examiner: Carlos Xisto, Department of Mechanics and Maritime Sciences

Degree project report 2024
Department of Mechanics and Maritime Sciences
Chalmers University of Technology
SE-412 96 Gothenburg
Sweden
Telephone +46 31 772 1000

Typeset in LaTeX
Gothenburg, Sweden 2024

Ice accretion in cryogenic heat exchangers
Dimensioning, building, testing and validating a heat exchanger rig for freezing condensate for various future aircraft engine applications
OLIVER KADI
Department of Mechanics and Maritime Sciences
Chalmers University of Technology

Abstract

As research into future concepts of aircraft propulsion advances, hydrogen-powered aircraft are becoming a considered alternative. Given that hydrogen fuel is extremely cold and could benefit from heating before combusting, and excess heat from the engine exists, a heat exchanger could benefit the overall efficiency of such an engine. However, freezing is thought to occur due to the humid air and the cold fuel flowing through the heat exchanger. This project will therefore aim to investigate ice accretion in a cryogenic heat exchanger.

To achieve this, a test rig must be dimensioned and constructed. Using a standard compact heat exchanger as described in Kays and London's Compact Heat Exchangers, the rig was drafted to replicate freezing conditions similar to those that could be expected in an aero engine. A parallel-running bachelor thesis ensured that the rig was constructed and functional in time for the testing phase of the project.

During the assembly of the rig, simulations in StarCCM+ were conducted, where icing effects were investigated using a multiphase model. The temperature drop used to dimension the heat exchanger was later compared to the observed results from the tests. The test results were visually compared to the ice propagation predicted by CFD.

Keywords: Heat exchanger, hydrogen, test, freezing, ice, StarCCM+, CFD, multiphase

Acknowledgements

First and foremost, I would like to express my thanks to my supervisor, Petter Miltén, who was great and guided me throughout the challenging task of investigating icing on heat exchangers. His guidance, advice, and support was invaluable. I highly appreciate his interest in the project. Additionally, I would wish him the best in his continued PhD studies.

I want to thank Anders Lundbladh for suggesting this thesis and making it all possible. As a supervisor from GKN Aerospace, his genuine interest in the project propelled the thesis forward. His knowledge and advice were greatly appreciated.

I would like to extend my gratitude to my colleague Pontus Miltén who worked tremendously hard on his parallel-running bachelor thesis. His efforts provided a platform to conduct the tests. Without him, the project would not have met its target.

A special thank you goes to Isak Jonsson for sharing his expertise in the lab. His experience was very helpful.

Finally, I extend my appreciation to my examiner, Carlos Xisto for his efforts, advice, and support throughout not only this project but also my Master of Science in Mobility Engineering, specifically in the Aerospace field.

Thank you all for your time and efforts!

Oliver Kadi
Gothenburg, June 2024

List of Acronyms

Below is the list of acronyms that have been used throughout this thesis listed in alphabetical order:

CAD	Computer Aided Design
CFD	Computational Fluid Dynamics
DMP	Dispersed Multiphase
HEX	Heat exchanger
HVAC	Heating Ventilation and Air Conditioning
Lam	Laminar
LH2	Liquid Hydrogen
NASA	National Aeronautics and Space Administration
NTU	Number of Transfer Units
Turb	Turbulent

Nomenclature

Below is the nomenclature of indices, sets, parameters, and variables that have been used throughout this thesis.

Indices

1,2,...	Indices for positions in rig
air	Index for defining that a variable is describing the fluid: air
cool	Index for defining that a variable is describing the fluid: glycol and water (coolant) mixture
c, h	Index for hot or cold
eff	Effective
f	Film
i,j	Index for phases in CFD sections
i,o	Index for outer or inner measurements
Lam	Index for laminar regime
max, min	Index for maximum or minimum
Turb	Index for turbulent regime
∞	Index for infinity

Parameters and Variables

A	Area of a certain surface
A_{fr}	frontal area of heat exchanger as described by Kays and Londons, Compact heat exchangers
C	Heat capacity rate of a fluid
c_p	Specific heat capacity of a fluid
D	Diameter, usually of a tube. It is expressed with indices to specify what diameter is being discussed

E	Total energy
$\boldsymbol{F}_{ij}^{D}$	Drag force that acts on the dispersed phase i due to the drag of phase j
f	Friction factor
$\boldsymbol{f}$	Body force vector
H	Total enthalpy
h	Heat transfer coefficient (usually convective). It is often seen accompanied by indices
k	Thermal conductivity
$k_{\text{eff},i}$	Effective thermal conductivity
L	Characteristic length
$\dot{m}$	Mass flow. Specified fluid is indicated by the index
NTU	NTU-number
Nu	Nusslet number
P	Pressure
p	static pressure
Pr	Prandtl number
$Q_{i,j}$	interphase heat transfer rate from i to j
q''	Heat flux
R	Radius of an object
r	Radial coordinate
Re	Reynolds number
RH	Relative humidity
St	Stanton number
S_E	Source term for energy equation in fluid film
$S_{u,I}$	Source term in continuity, momentum and energy equations
T	Temperature of specific fluid or object or phase
$\boldsymbol{T}$	Viscous stress tensor
u	Velocity of fluid
V	Volume defined in the index
V	Volume of cell in CFD section
V_i	Volume of phase i in CFD section
V_f	Volume of film in CFD section
$\boldsymbol{v}_i$	Velocity of phase
$\boldsymbol{v}_f$	Velocity of film

α	The ratio of the total transfer area
α	The volume fraction in the CFD section
Δ	Describes a change in a specific variable
ϵ	Effectiveness of heat exchanger
η	Ratio of volume that is occupied by all continuous phases to the total cell volume
η^*	Available volume fraction from the previous iteration or time step
μ	Dynamic viscosity of specific fluid
ρ	Density of specific fluid
σ	Void fraction

Contents

List of Figures

List of Tables

1

Introduction

As the research into the next generation of aviation engines is growing the introduction of sustainable alternatives to existing concepts is being considered. Such advancements can be brought forward by increasing the efficiency of engines through extracting more useful work or by replacing the fuel type used, which in turn reduces the impact on the environment. This section will provide the necessary background for hydrogen-powered aircraft and the introduction of heat exchangers in these applications. The purpose, goals, and delimitations will be introduced as well.

1.1 Background

Liquid hydrogen is being considered as a substitute fuel for future airplanes in alignment with the target set by the European Union Green Deal, which aims to no net greenhouse gas emissions by the year 2050 [1]. Generally, there is an increased interest in research in such a field and the advantages of adopting such a fuel have been seen to be advantageous for both long and short-range aviation [2] [3]. The usage of liquid hydrogen (LH2) storage provides a better energy density compared to compressed gas [4]. It can be indicated through previous studies that hydrogen should be stored under cryogenic conditions, this could produce possible issues that need to be investigated further [5].

Heat exchangers (HEX) transfer thermal energy between two or more fluids, usually through a solid material separating them [6]. Heat exchangers are mostly used for cooling critical components but the energy of a machine can be utilized to increase the overall efficiency of the machine. In the case provided by GKN Aerospace, this could be cooling down aero-engines humid air with the help of a cold fuel such as liquid hydrogen. The fuel in this case is extremely cold (20 K at atmospheric pressure) and depending on where the heat exchanger is implemented the hot air could range from 300 K to around 700 K. Using a heat exchanger to lower the temperature of various sections of this humid air through the utilization of liquid hydrogen appears to offer potential advantages [7]. The range of applications can consist of implementations in between compressors as intercoolers as it would raise the fuel temperature before entering the combustion chamber and reduce the compressor's work by cooling the airflow [8]. Potentially such heat exchangers could also be used after the combustor to avoid the risk of melting turbines due to the high temperatures experienced after combusting, such solutions could be seen in Fig. 1.

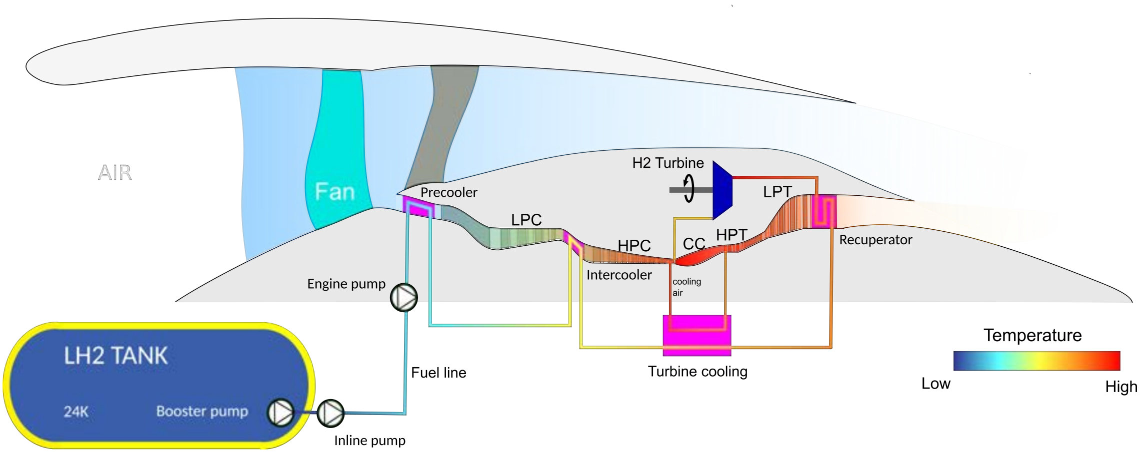

Fig. 1. Figure demonstrating possible usages of heat exchangers in an aero-engine [8]. Reproduced with permission.

Icing could therefore occur in liquid hydrogen heat exchangers. Although no specific cases match the criteria an aircraft engines, some research into icing has been conducted in everyday usage cases such as Heating Ventilation, and Air Conditioning (HVAC) systems. This leads to some speculations on what could happen on a liquid hydrogen heat exchanger, including reduced operational efficiencies [9] [10].

1.2 Purpose

The objective of this project is to develop a test rig specifically designed for the experimental investigation of ice accretion in a compact heat exchanger. The constructed rig will be used to gather data and establish relationships to predict ice formation when implemented in real engines. Computational fluid dynamic calculations will be provided to compare to the test scenario allowing for some prediction before conducting the physical tests.

1.3 Scope

The scope of the thesis revolves around the experimental investigations to be carried out. Supporting numerical analysis will be conducted for comparison and clarification on the conducted investigation. This will include the limitations of this project including time, resources, and work needed to satisfy the core objective.

1.3.1 Clarifications on the Objective

A facility for testing the freezing of humid air in heat exchangers will be built. The project will aim to size the testing rig to the requirements defined at the beginning of this project. It will also provide a platform on which data gathering and deeper investigation into the relations between icing and heat exchanger characteristics. Finally, a CFD environment is set up to investigate the similarity to the gathered data.

1.3.2 Delimitations

The project will take place during the time available for the master thesis which consists of 20 weeks, where the starting date is the 19th of January 2024 and the preliminary internal deadline of the report is set to the 5th of May as the project is in parallel with a Bachelor's thesis. The remaining time is planned to extend to the latest to the 9th of June. This can be seen in the Gannt-scheme in appendix H.

The rig will be built at the Chalmers Laboratory of Fluid and Thermal Sciences with a set budget. The measurements and data gathered will have to be conducted with the available facilities. If necessary equipment will be bought for the rig to be built.

The optimization of components such as heat exchangers, ducts, fans, or other components will not be investigated. The focus is rather to dimension a rig that provides a range of flexibility to test different configurations in a short amount of time. The rig will be designed so that the results are reliable and trustworthy. The initial design of the rig will include one configuration of a tube cross-flow heat exchanger, but this does not limit future applications to implement other types of heat exchangers. The numerical investigation in CFD will utilize standard and recommended practices. This means no efforts will be put into improving or adjusting the solvers or models.

1.4 Test Rig

The heat exchange rig will consist of two loops, the air loop, and the coolant loop, which can be seen in Fig. 2. In addition to the mentioned sections, instrumentation for observation and measurements is needed and will be brought up in this section. The system can be broken down and represented in the sketch seen in Fig. 2.

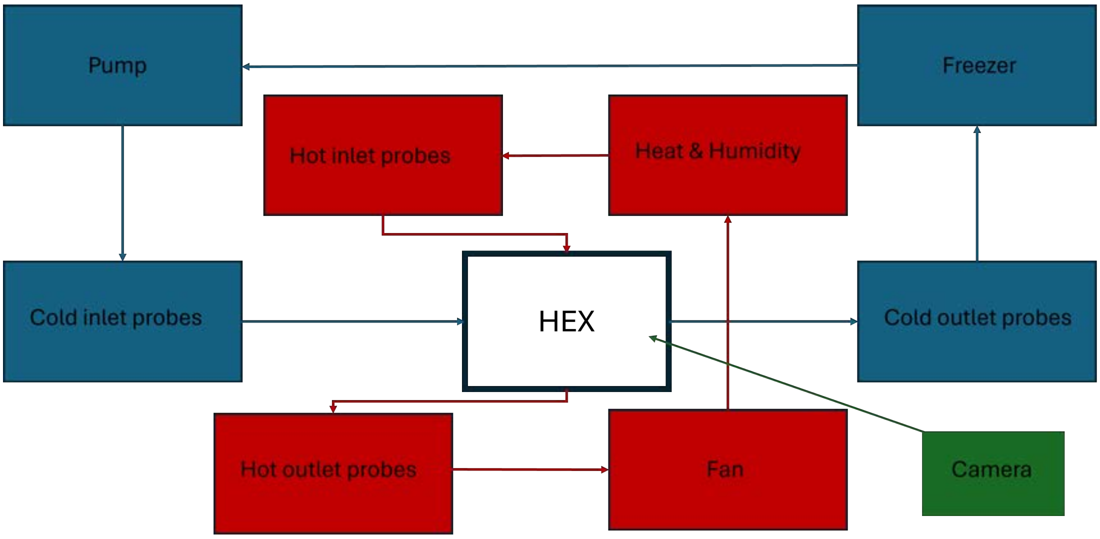

Fig. 2. Schematic representing the basic layout of heat exchanger circuits.

1.4.1 Air Section

The air section is dictated by the Reynolds number desired and flow characteristics achievable in an aero-engine HEX. These conditions should therefore cause ice accretion in the HEX test section. As a tubular HEX is investigated in this project flow dynamics around rows of staggered tubes is a crucial part of the air loop. A singular tube will exist in an unseparated regime for low Reynold number (under Reynolds number 5), as Reynolds increases the separation and wake vortices increase until the vortex wake is laminar and periodic. As the Reynolds number increases further the flow transitions into a turbulent flow regime at $Re \approx 3000$. This will result in time-dependent flow conditions. It is thought that this high Reynolds number behavior, seen in Fig.1 in [11], will be observed in the conceptual aero-engine this project is considering.

For rows of tubes in applications such as heat exchangers, heat transfer and friction are not notable before a higher Reynolds number (roughly 2000 in [12]). In staggered configurations where the second row of downstream tubes sits in between the upstream the effects of heat transfer are increased. In heat exchanger experiments such as the works of Kays and London Reynolds numbers above 15000 and below 300 do not seem to be of interest for tube heat exchangers, as can be seen in Table 10-2 in [13]. This indicates that the constructed air section for this rig should fall somewhere in this range. In addition, it can be deduced by the heat transfer equations in section 2.1 (eq. 2.5) that in broad terms a lower Reynolds number will cool the air more moving through the tubes, which suggests if the icing is to be induced it can be beneficial to run the test rig in lower air speeds.

Whereas for the air stream outside the test section, the design should be considered carefully before proceeding with the design of the air system. A poorly thought-out air system could provide uncertain flow conditions and unaccounted phenomena, such as undeveloped flow, uneven flow throughout the cross-section, and unaccounted-for losses. As can be seen in Fig. 2 probes into and out of the HEX are needed to control the desired conditions. This means pressure and temperature are to be measured and would yield sufficient information on the air system in a non-humid condition. As this project will consider humid air, humidity needs to be delivered and controlled into the wind tunnel. Two types of wind tunnels can be considered: A suction fan with a bell-mouth configuration in a closed box where the ambient temperature in the box or room is controlled, or a climate wind tunnel with a closed loop configuration.

1.4.2 Coolant Section

For the coolant fluid, as the temperatures are subzero it is important that the liquid does not freeze. The viscosity does not significantly change throughout the experiment as the temperature change is limited to be close to one degree. The coolant side should be dimensioned in a manner that it is possible to force freezing in the rig. This would be validated through the heat transfer calculations shown in 2.1. The coolant section should also provide a cooling effect needed for a reasonable duration of test time to measure substantial ice buildup. As a heat exchanger would have several tubes a clever management system that allows for correct flow characteristics is necessary. This manifold construction should ensure similar flow throughout all tubes whilst minimizing pressure and friction losses. A manifold will simplify the construction and assembly of the test section.

2

Theory

To gain a thorough picture of heat exchangers within the scope of this project, it is important to establish the fundamentals of heat exchangers. Specifically clarifying the underlying physics of condensation and freezing processes. These mechanisms are not only essential to comprehend the workings of the test rig but also for the subsequent section involving numerical solutions using computational fluid dynamics.

2.1 Fundamentals of Heat Exchangers

This section aims to provide the necessary background for heat exchangers. It will demonstrate some types of HEX, boundary layer importance, the specific dimensionless numbers used in heat exchangers, heat transfer equations, and the ϵ-NTU method of designing heat exchanges.

2.1.1 Types of Heat exchangers

Heat exchangers can be divided into three groups: Parallel flow, counter flow, and cross flow. Each provides its unique capabilities and is beneficial in different scenarios. The three can be visualized in Fig. 3. Cross- and counter-flow exchangers are more common in today's applications since parallel flow HEX produces worse heat transfer. Counter flow is generally considered the most preferred, whereas cross flow is simpler to implement.

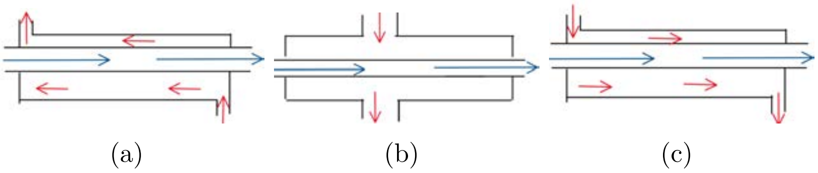
(a) (b) (c)

Fig. 3. (a) Counter flow, (b) Cross flow, (c) Parallel flow heat exchangers shown in sketches.

Some common heat exchangers house the second fluid using circular or flat tubes. The heat exchangers can have fins in either circular or plate format. In this project, tube heat exchangers without fins will be considered for the most part but extensive research exists on all configurations.

In cross-flow HEX there will naturally exist a cold corner [9]. This corner will be where the coolant enters the system and the hot air is about to leave, hence cooled down.

2.1.2 Boundary Layers

Correctly modeling the thermal and viscous boundary layers in heat exchangers is highly important. The narrow flow passages found in compact HEX result in a high ratio of boundary layer to bulk flow. In Fig. 4 the velocity and thermal boundary layers can be displayed in laminar, transitional, and turbulent flows, where u represents the velocity of the flow and u_∞ represents the free stream velocity. Similarly for the thermal boundary layer can be represented by u, where T_∞ is the temperature in the free stream fluid.

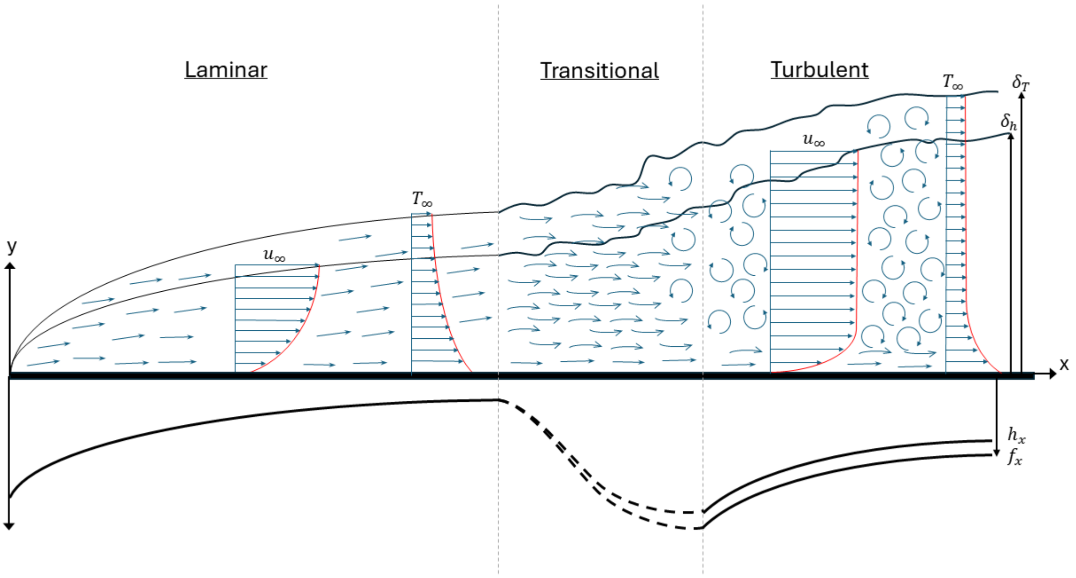

Fig. 4. Figure representing the velocity and thermal boundary layer growth in different flow regimes. (Recreated and adjusted based on Fig.6.6 in [14]).

2.1.3 Dimensionless Numbers

To define the flows across a heat exchanger, several different dimensionless numbers need to be introduced. The most common of which is the Reynolds number denoted Re. The Reynolds number in heat exchangers is expressed as usual depending on the velocity, density, characteristic length, and viscosity usually depicted in the following form:

$$Re = \frac{\rho u L}{\mu} \tag{2.1}$$

The Reynolds number itself is used to describe the type of flow being observed in Fig. 4 above. For heat exchangers the Pradntl number can be defined as a parameter used in heat transfer calculations between a fluid in motion and a stationary particle. The Prandtl number is derived from the ratio of heat transfer to skin friction within the turbulent boundary layer [15]. The Prandtl number, Pr, can therefore be expressed as the momentum diffusivity by the thermal diffusivity, in other words as follows,

$$Pr = \frac{c_p \mu}{k} \tag{2.2}$$

where k is the thermal conductivity. Another essential non-dimensional heat transfer coefficient known as the Nusselt number, Nu, is defined as the ratio of total heat transfer to conductive heat transfer across a boundary. The Nusselt number is often seen as

$$Nu = \frac{hl}{k} \tag{2.3}$$

where h is the heat transfer coefficient. As a product of all the mentioned the Stanton number, St is written as

$$St = \frac{Nu}{Re \times Pr} \tag{2.4}$$

2.1.4 Heat Transfer Across Heat Exchangers

To determine the size of the HEX it can be beneficial to understand the heat transfer equations. The heat transfer will ultimately decide the change in temperature across the rig and therefore impact the dimensioning of it. Here U is defined as the overall heat transfer coefficient of the exchanger and is written as,

$$U_{air} = 1/\left[(\frac{1}{h_{air}}) + \left(\frac{D_{outer} - D_{inner}}{(A_w/A_{air})k_{wall}} \right) + (\frac{1}{(A_c/A_{air})h_{coolant}}) \right] \tag{2.5}$$

Here U_{air} consists of the heat transfer coefficient of air, wall, and coolant (seen in the mentioned order in the expression above). The inner and outer diameter of the tube is denoted by D with respective subscripts. The thermal conductivity k is a material parameter that determines the transfer of heat and in this case, is assumed constant for aluminum tubes. The term A is the heat transfer area of the respective region determined by the subscript, w for the wall. For air and coolant, this area can be expressed as the ratio of the total transfer area on one side of the exchanger to the total volume of the exchanger.

$$A = \alpha V \tag{2.6}$$

where V is the total volume of the heat exchanger. The ratio, α is defined as the ratio of the total transfer area on one side of the exchanger to the total volume of the exchanger. The individual heat transfer coefficient h is determined by eq. 2.3.

2.1.5 Sizing of Compact Heat Exchangers

A common design method when sizing a HEX is the ϵ-Ntu method [15] [13]. Here the concepts of heat transfer and the previously discussed dimensionless numbers are used to set conditions for heat exchangers. The interesting factors dimensioning a heat exchanger in this case can be summed to the temperature and pressure differences created in certain inlet configurations. As seen in Fig. 4 the heat transfer coefficient is highly dependent on the flow regime. The relations for friction factor (f) and heat transfer coefficient (h) are derived from the Gnielinski correlation. The friction factor in the tubes is calculated according to the following criteria

$$f = \begin{cases} \frac{64}{Re} & \text{if laminar} \\ (0.79\log(Re) - 1.64)^{-2} & \text{if turbulent, according to Petukhov [16].} \end{cases} \tag{2.7}$$

Whereas the friction factor on the air side is determined through correlations from Kays and London (seen tabulated in Appendix B or in [13]). Then the heat transfer coefficient is found through eq. 2.3 expressing it for h. Nu on the air side is found through the mentioned dimensionless numbers in equations 2.3, 2.2, and 2.1. Whereas for liquid in tubes, it is defined according to Gnielinski [17], this results in Nu being expressed in the two following forms

$$Nu = \begin{cases} StRePr & \text{on air side} \\ (1 - \frac{1}{(1+\exp(-k(Re-Re_{MidPoint})))})Nu_{Lam} + \frac{1}{(1+\exp(-k(Re-Re_{MidPoint})))}Nu_{Turb} & \text{inside tubes.} \end{cases} \tag{2.8}$$

Here the subscripts depict which flow regime the dimensionless number corresponds to. The subscript MidPoint refers to the midpoint between laminar and turbulent regimes in terms of Reynolds numbers. $Re_{midpoint}$ is set based on analytical data that suggests around 2300-3000 is when the flow transitions to turbulent. The transitional $Re_{midpoint}$ is 2700 in this case as it is the midpoint of the transitional flow. In this case, the Nusselt number for laminar flows can be determined by a constant whereas in the turbulent regime can be expressed as

$$Nu(\text{Inside tubes}) = \begin{cases} 3.66 & \text{if laminar} \\ \frac{(\frac{f_{Turb}}{8})(Re-1000)Pr}{(1+12.7(\frac{f_{Turb}}{8})^{0.5})(Pr^{(2/3)}-1)} & \text{(Gnielinski correlation [17])if turbulent.} \end{cases} \tag{2.9}$$

where the Gnielinski correlation is valid for $3000 < Re < 5 \cdot 10^6$ and $0.6 < Pr < 105$. The pressure losses on the air side can then be found by utilizing equations in [13] and is written as,

$$\Delta P = \frac{\dot{m}^2}{2A_{fr}^2}[(\frac{1}{\sigma^2} + 1)(\frac{1}{\rho_2} - \frac{1}{\rho_1}) + f\frac{\alpha}{\sigma^2}L\frac{1}{\rho_m}] \tag{2.10}$$

where σ is the void fraction. The dimensionless numbers on the air side for the compact HEX can be found through the work of Kays and London, where the values are provided based on a set of experimental tests conducted [13]. Whereas for the coolant side, these values are found through correlations such as the Gnelinski correlation used in this case. To simplify, ΔP_{cool}, the pressure change inside a tube can be derived from eq. 2.10 and be written as

$$\Delta P_{cool} = f\frac{L}{D}\frac{\rho v^2}{2} \tag{2.11}$$

The heat transfer is found through the ϵ-NTU method. By finding the maximum NTU number (NTU_{max}) and defining the effectiveness, ϵ. For air-to-liquid cross-flow HEX, the effectiveness equation can be simplified to the following

$$\epsilon = 1 - \exp(-NTU_{max}). \tag{2.12}$$

The maximum NTU number can be found by dividing the product of the total volume, V, and α_{air} by the minimum heat capacity rate, C_{min}. Therefore the maximum NTU number is expressed as

$$NTU_{max} = \frac{V\alpha_{air}U}{C_{min}} \tag{2.13}$$

To define C_{min} the heat capacity rate for air and coolant can be defined as

$$C = c_p * \dot{m} \tag{2.14}$$

where c_p is the specific heat and $\dot{m}$ is the mass flow of the fluid in interest. Therefore C_{max} and C_{min} is the maximum or minimum value of the corresponding heat capacity of the two fluids. The temperature difference can then be expressed as

$$\Delta T = \begin{cases} -\epsilon(\frac{C_{min}}{C_{air}}(T1_{air} - T1_{coolant}) & \text{air} \\ \epsilon(\frac{C_{min}}{C_{coolant}}(T1_{air} - T1_{coolant}) & \text{coolant} \end{cases} \tag{2.15}$$

2.2 Condensation and Freezing

Condensation is thought to be observed before freezing, hence understanding how condensate forms is crucial for the icing procedure. Icing is expected to form due to condensate but also other factors and is therefore another interesting phenomenon that will be discussed in this section.

2.2.1 Condensation

Condensation can occur in two ways, the dominant form, is where a liquid film covers the entire condensation surface and can be seen in both Fig. 5(A) and Fig.10.10 in [14]. Film condensation as it is called, is generally a characteristic observed in uncontaminated surfaces. The other case is dropwise condensation which forms in cracks, pits, cavities, or if the surface is coated with some agent that prevents wetting. Since the tubes to be used in the experimental investigation are assumed clean and without the mentioned causes of dropwise condensate, a film condensate will be assumed. This decision will be especially relevant for CFD applications.

Another aspect to be considered regarding film condensation is whether it exists in a laminar or turbulent regime as described in Chapters 10.7 and 10.8 in [14]. In terms of heat transfer, this indicates that there will be a new interface between the surface and the humid air. This condensate film will have its thermal transfer and behave differently from a heat exchanger that does not experience condensation. The specific condensation and convection phenomena can be seen in Chapters 10.2 and 10.3 of Fundamentals of Heat and Mass transfer [14].

Most importantly for tube heat exchanger, is how the condensation acts when several rows of tubes exist. In essence, due to the existence of a film convention upstream, the effects will carry on onto the tubes downstream and so on for the entirety of the heat exchanger. The reduction of heat transfer is said to increase with the number of rows or columns due to the films impacting each other. There exist two methods of viewing the stream, a continuous condensate sheet and dripping condensate, see Fig. 5. For tube banks, it is mostly assumed that the condensate falls in a continuous sheet. Two effects are neglected, heat transfer to condensate sheet between tubes and momentum gain as the sheet falls [14]. These assumptions tend to result in lower values than the experimental results, where an argument could be made that the dripping condensate would be a more relevant explanation. Dripping causes turbulence and reduces the condensate film thickness.

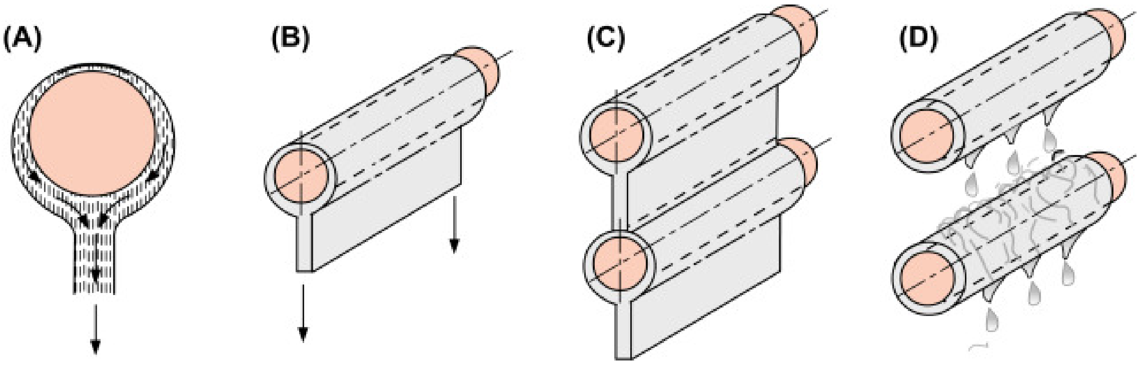

Fig. 5. Figure representing condensate on (A) a sphere, (B) a single horizontal tube, (C) a vertical tier of horizontal tubes with a continuous condensate sheet, and (D) with dripping condensate (Fig.3.15 in [18]).

2.2.2 Freezing

As condensate forms, two major things might occur: continuous condensate pooling in the bottom of the heat exchanger, or if enough heat transfer is provided freezing. Some limited research has been made on the freezing of heat exchangers mostly in HVAC applications, but extensive experimental and numerical data has been gathered on the freezing of airplane wings.

In airplane applications where freezing occurs on bodywork such as wings, it usually propagates from the leading edge. This is confirmed by the works of NASA where the repeatability of ice propagation was tested in ranges of -15°F to 28°F [19]. Several other experimental studies on the icing of airfoils have been conducted that explain the ice propagation throughout different flow angles which can be used to understand icing on tubes in heat exchangers [20]. Ice propagation is heavily researched and the most common form seen is the icing starting from the stagnation point. Investigation on the dynamic ice accretion and unsteady heat transfer over an airfoil can be seen in [21]. CFD simulation software, such as StarCCM+, have conducted studies where the software's capability of predicting ice has been compared to experimental results [22]. This provided a reason for using this software specifically. More about the CFD software can be seen in the coming section.

As mentioned in section 2.1.1 the existence of a cold corner will therefore, with good reason, predict that ice will propagate from that corner first [9]. In the mentioned Hoval report [9], a simple finite element method supports this hypothesis. Cross-flow air-to-air heat exchangers for energy recovery are also studied and for such cases, ice formation is calculated thoroughly using mathematical models in [23]. Condensation and ice build up will therefore change the heat exchanger's performance and result in increased difficulty in both heat transfer and pressure loss predictions. For example, the change in both the thickness of the tube and k in equation 2.5 will impact U.

2.3 CFD

This section will focus on the specific areas of a CFD setup for icing of heat exchangers and will highlight the three most important physics conditions: Boundary condition, Dispersed Multiphase Flow, and Fluid films. In Appendix D a detailed setup section will be attached for a general explanation of the simulation file.

2.3.1 Boundary Conditions

In computational fluid dynamics, the types of boundary conditions used are important for the accuracy of the solution. One way of determining the boundary condition is by setting a solid face to be a constant temperature and therefore transfer heat accordingly. Another can be to consider the inside of the solid, in this case, the inside of a tube, to have a constant temperature. Finally, the temperature could be found through calculating the liquid heat transfer into the wall and then into the air. The complexity of the boundary condition will vary the results and time to simulate. It is therefore important to choose appropriate boundary conditions.

Constant tube temperature

This is the most common starting point of heat transfer simulations. It provides simple conditions to fulfill, but in reality might not be completely true, due to losses that can be calculated according to sections 2.1.4 and 2.1.5. In this case, the boundary condition can then be expressed as follows,

$$T(r = R) = T_{wall} \tag{2.16}$$

where r denotes the radial coordinate and R denotes the tubes radius. In the following experiments, this can be a reasonable assumption as the liquid inside the tubes has a high heat transfer capacity and the tube is considered thin. The experiment must therefore only ensure a constant or near-constant temperature across the tube. In this thesis, the assumed temperature is the measured temperature inside the inlet and outlet of the liquid coolant.

Constant inner tube temperature

This boundary condition assumes that the inside of the tube has a constant temperature and that the tube is relatively thin-walled. The heat flux, $q\prime\prime$, will be expressed as

$$q\prime\prime = \frac{dT}{dR}(R_{+}) \tag{2.17}$$

and the thermal conductivity in air, k_{air}

$$k_{air} = \frac{dT}{dr}(r = R)k_{wall} \tag{2.18}$$

where R_{+} is the value at the radius towards the air side.

Calculating temperature

A boundary condition where the temperature is calculated by using the temperature of the fluid in the tube the thermal conductivity of the tube, wall thickness, and the thermal conductivity in air. This will result in its simplest form an expression in the form

$$T(r = R) = T_{fluid} + k_{air}t_{wall}\frac{dT}{dr}(r = R_{+})k_{air} \tag{2.19}$$

where, in this case, T_{fluid} is considered as the average temperature of the coolant over the cross-section of the flow in the tube. With eq. 2.19 it is therefore possible to calculate only on the air side of the heat exchanger. This can be combined with eq. 2.17 and 2.18 but requires a mesh and computational power for the tube. Instead, an estimation constant can be used as the heat transfers between the fluid to the inside of the tube. In this case, with the assumption of a thin wall, the following boundary condition can be deduced,

$$T(r = R) = T_{fluid} + \frac{dT}{dr}(r = R_{+})k_{air}/u_{fluid-wall} + k_{wall}t_{wall}\frac{dT}{dr}(r = R_{+})k_{air} \tag{2.20}$$

in other cases where a thin wall can not be assumed a term for the wall thickness can also be used to compensate. As a start, this project will consider constant temperature boundary conditions for cases where CFD is used to compare test results.

2.3.2 Dispersed Multiphase Flows (DMP)

The dispersed multiphase model simulates the flow of dispersed particles in an Eulerian approach. By default, DMP is one-way coupled but can use two-way coupling if needed. For each dispersed phase StarCCM+ solves the transport equation for the conservation of mass and momentum. The following governing equations and further documentation can be found in the Simcenter StarCCM+ 2302 user guide under Theory in [24].

Volume Fraction

As multiphase flows consider multiple phases the volume fraction is considered to be one of the governing equations. In DMP this can be written as

$$V_i = \int_V \alpha_i dV \tag{2.21}$$

where V is the volume of the phase i and α_i is the volume fraction. The available volume fraction of the continuous phase can be related to the dispersed phase by the following equation

$$\eta = \eta^* + (1 - \frac{V_i}{V}) \tag{2.22}$$

where η^* is the available volume fraction from the previous time step or iteration and V expresses the volume of the cell.

Continuity Equation

For phase i the continuity equation can be noted as

$$\frac{\partial}{\partial t} \int_V \alpha_i \rho_i dV + \oint_A \alpha_i \rho_i \boldsymbol{v}_i \cdot d\boldsymbol{a} = S_{u,i} \tag{2.23}$$

where α represents the volume fraction, ρ the density, $\boldsymbol{v}$ the velocity, and $S_{u,i}$ a defined mass source of the phase i.

Momentum Equation

The momentum equation for the DMP model is given as

$$\frac{\partial}{\partial t} \int \alpha_i \rho_i \boldsymbol{v}_i dV + \oint_A \alpha_i \rho_i \boldsymbol{v}_i \otimes \boldsymbol{v}_i \cdot d\boldsymbol{a} = - \int_V \alpha_i \nabla p dV + \boldsymbol{F}_{ij}^D + S_{u,i} \tag{2.24}$$

where p is the static pressure, $\boldsymbol{F}_{ij}^D$ the drag force that acts on the dispersed phase i as a result of the drag of the other phase j, and $S_{u,i}$ a defined momentum source.

Energy Equation

Finally, the energy equation for the DMP model can be seen in

$$\begin{aligned} &\frac{\partial}{\partial t} \int_V \alpha_i \rho_i E_i \, dV + \oint_A \rho_i H_i \boldsymbol{v}_i \cdot d\boldsymbol{a} + \oint_A \alpha_i p \, d\boldsymbol{a} \\ &= \oint_A \alpha_i k_{\text{eff},i} \nabla T_i \, d\boldsymbol{a} + \oint_A \boldsymbol{T}_i \cdot \boldsymbol{v}_i \, d\boldsymbol{a} + \int_V \boldsymbol{f}_i \cdot \boldsymbol{v}_i \, dV \\ &\quad + \int_V \sum_{j \neq i} Q_{i,j} \, dV + \int_V S_{u,i} \, dV \end{aligned} \tag{2.25}$$

where E_i is the total energy, H_i the total enthalpy, $\boldsymbol{T}_i$ the viscous stress tensor, T_i the temperature, $k_{\text{eff},i}$ the effective thermal conductivity, $\boldsymbol{f}_i$ the body force vector, and $Q_{i,j}$ the interphase heat transfer rate to phase i from j.

2.3.3 Fluid film

A fluid film allows the simulation of a thin layer of liquid film on a solid surface. This application is relevant for condensation and solidification which also includes droplet impingements of the DMP phase. The fluid film can change throughout the simulation and StarCCM+ achieves this by solving the transport equations for mass, momentum, energy, and species in the tangential direction. In this case, it assumes a piecewise linear profile, for temperature and species across the fluid film. As in the previous section, this information can be found in the Simcenter user guide under Theory in [25].

Volume fraction

The film volume is subtracted from the volume of the gas phase in the neighboring cell to the film and the volume fraction of the film in the neighboring gas cell is expressed as

$$\alpha_f = \min\left(\frac{V_f}{V}, \alpha_{f,max}\right) \tag{2.26}$$

where V_f is the film volume, V the volume of the neighboring cell, and $\alpha_{f,\text{max}}$ the maximum volume fraction.

Continuity Equation

The governing equation for mass conservation can be noted as

$$\frac{\partial}{\partial t}\int_V \rho_f dV + \int_A \rho_f \boldsymbol{v}_f \cdot d\boldsymbol{a} = \int_V \frac{S_u}{h_f} dV \tag{2.27}$$

where ρ_f is the film density, $\boldsymbol{v}_f$ the film velocity, and S_u the source term. In this case, contributions to the source term can be droplet impingement, film stripping, mass transfer, or even pre-defined conditions.

Momentum equations

Conservation of momentum for a fluid film can be expressed as follows

$$\frac{\partial}{\partial t}\int_V \rho_f \boldsymbol{v}_f dV + \int_A \rho_f \boldsymbol{v}_f \otimes \boldsymbol{v}_f \cdot d\boldsymbol{a} = \int_A \boldsymbol{T}_f \cdot d\boldsymbol{a} - \int_A p_f d\boldsymbol{a} + \int_V \left(\boldsymbol{f}_b + \frac{\boldsymbol{s}_m}{h_f}\right) dV \tag{2.28}$$

where $\boldsymbol{s}_m$ can be defined as the momentum source corresponding to the mass source S_u, p_f as the static pressure, $\boldsymbol{f}_b$ as the body force vector, and $\boldsymbol{T}_f$ as the viscous stress tensor in the film. The kinematic and dynamic conditions at the interface should satisfy equilibrium such that, for example, the velocity on the fluid film interface should equal that in the gas interface. Otherwise, these conditions relate to the surrounding fluid.

Energy Equation

The energy equation is finally given as

$$\frac{\partial}{\partial t}\int_V \rho_f E_f dV + \int_A \rho_f H_f \boldsymbol{v}_f \cdot d\boldsymbol{a} = \int_A \boldsymbol{q}_f{''} \cdot d\boldsymbol{a} + \int_A \boldsymbol{T}_f \cdot \boldsymbol{v}_f d\boldsymbol{a} + \int_V \boldsymbol{f}_b \cdot \boldsymbol{v}_f dV + \int_V \frac{S_E}{h_f} dV \tag{2.29}$$

where E_f is the total energy, $\boldsymbol{q}_f{''}$ the total enthalpy, and $\boldsymbol{T}_f$ the viscous stress tensor of the film. The body force per unit volume is defined as $\boldsymbol{f}_b$ and the energy source term as S_E.

3

Methods

The project began with sizing the test rig according to specifications and calculations accounting for ice accumulation. Subsequently, the rig was built, and CFD cases were established to anticipate the behavior of the tests. The project then concluded with the execution of tests and data collection.

3.1 Initial Sizing of Test Rig

A HEX geometry was provided from Kays and London [13], specifically the S150-125, a cross-flow tubular HEX. With this HEX, preliminary estimations were conducted through hand calculation where major assumptions were taken as seen in appendix A. These estimations were initially used to achieve an understanding of the requirements of the test facility.

With a fundamental understanding of the possible size of the test rig, the sizing investigation commenced. This was done by developing a Python script that used correlations and experimental data to investigate the pressure loss and heat transfer for various mass flows. The correlations used for the air section were based on the values provided by Kays and London seen in appendix B. The values were interpolated for the swept mass flows. Whereas for the coolant side, the heat transfer and pressure loss were determined through correlations mentioned in the previous section. This determined a possible range of operations that further set dimensioning requirements on the selection of equipment such as the pump and fan. The procedure can be visualized in the following steps, where all tubes are cooled and enforcing the conditions in Tab. II.

TABLE I
CONDITIONS FOR INITIAL CALCULATIONS

$T1_{air}$	T_{cool}	**Cp and k**
50 $°C$	-20 $°C$	constant

It is possible to produce pressure loss graphs for both air and coolant massflows respectively.

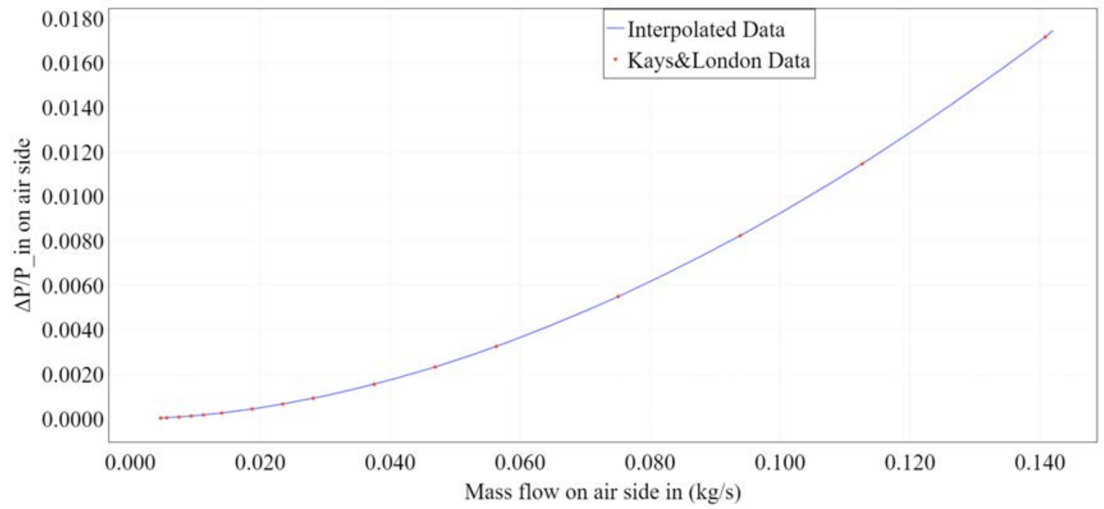

Fig. 6. ΔP by inlet pressure as a function of air massflow.

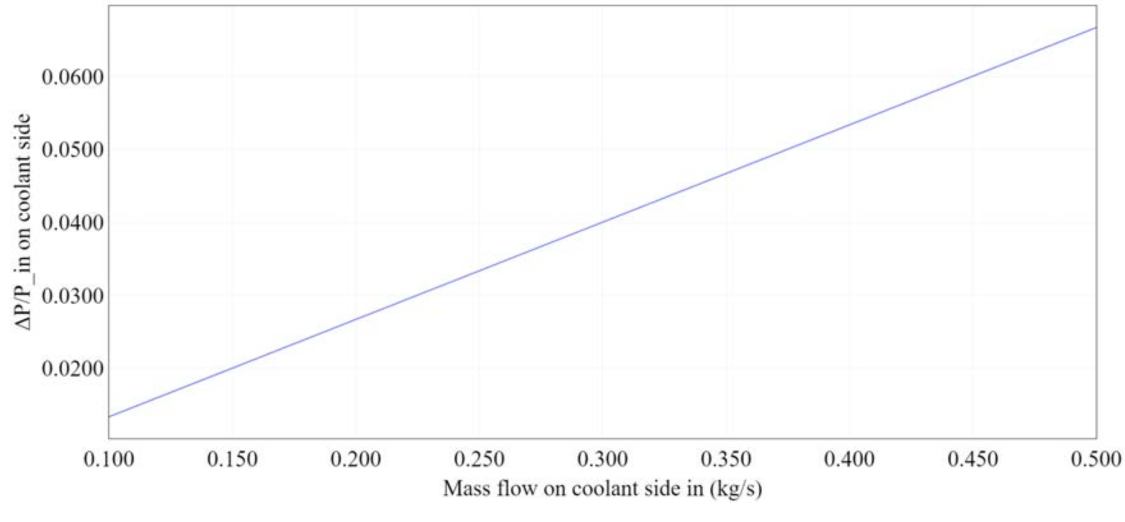

Fig. 7. ΔP by inlet pressure as a function of coolant massflow.

Fig. 6 - 7 showcase the range of mass flows and the resulting pressure drops, which dimensioned the HEX rig. The temperature difference, ΔT can be shown as a color map with the coolant massflow on the x-axis and the air massflow on the y-axis.

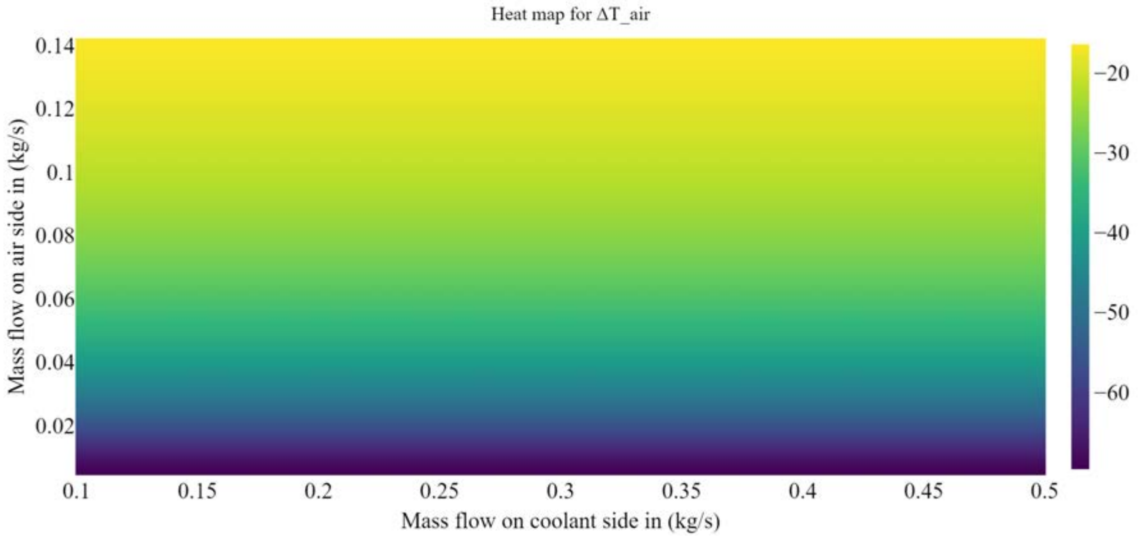

Fig. 8. Color map showing the change in temperature on the air side across various mass flow combinations.

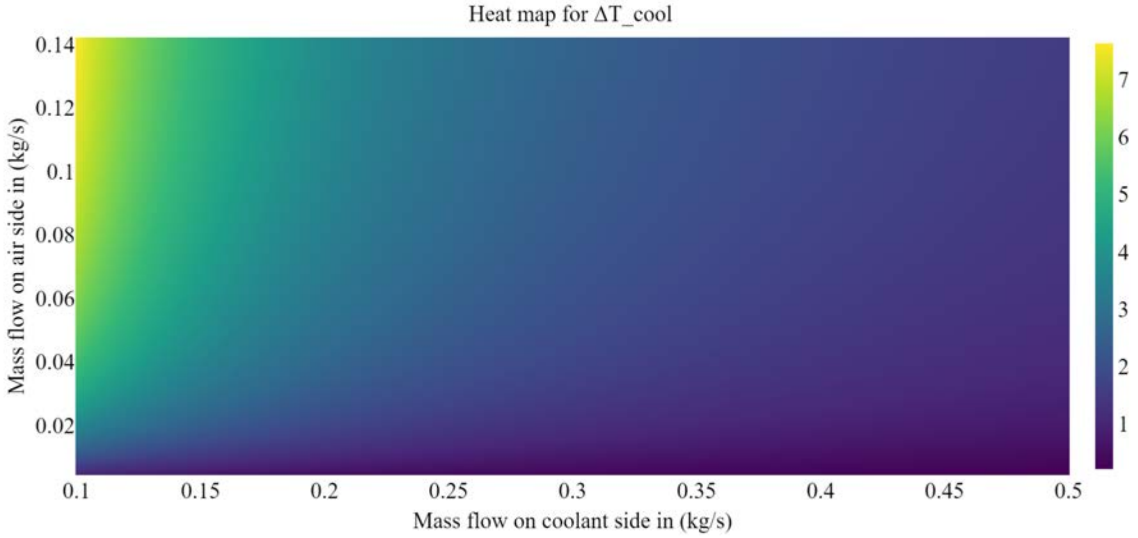

Fig. 9. Color map showing the change in temperature on the coolant side across various mass flow combinations.

With these graphs, it is possible to dimension the rig and additional components that will provide such behaviors in the rig.

3.2 CFD Simulation Setup

The CFD domain was built up sequentially, where the first cases focused on the understanding of models and physics, the steps used while constructing the simulation file can be summarized in the following points:

1. Partial section of heat exchanger with tubes upstream and with arbitrary physics conditions in the environment
2. Entire rig with partial cooling effects on tubes. Only three rows of tubes cool the system. With arbitrary physics
3. Validation case: Using the same case as the rig to investigate the validity of the CFD simulations.

The detailed simulations setups is available in appendix D. A simple mesh study was conducted to verify the convergence of the results. The boundary conditions consisted of a velocity inlet which determined the inlet flow into the test section and would be set according to the observed measurements in the rig. As mentioned in section 2.3 the technique involved uses multiphase physics, which requires an implicitly unsteady simulation. The inlet conditions were then set and the results were compared to the experimental investigation. The criteria for the full domain can be summarized in the table below:

TABLE II

Mesh size [cells]	**Maximum y+**	**Turbulence model**
$3.2 \cdot 10^6$	Target: <1	k-ω SST

As remeshing and adaptive meshing were used to ensure that no zero-volume meshes were created during ice accretion the number of cells changed. The y+ also changed resulting in non-physical values such as negative values by the end of the simulation. The inlet was considered a velocity inlet and the outlet was set to the boundary condition outlet. This was chosen as the velocity in the inlet is known and the conditions in the outlet are unknown. The symmetric domain symmetry was chosen for the side walls, whereas the full domain was modeled as walls since it aimed to simulate the test case. The cooled tubes were set to the constant temperature boundary condition mentioned in section 2.3.1. The implicitly unsteady solver was of first order and the flow was solved using the segregated flow model SIMPLE. As this is a multiphase problem the multiphase gas model was chosen and split up into water (H20) and air, where the mass fraction of each was selected according to the desired relative humidity.

3.2.1 Dispersed Multiphase Flows (DMP)

Icing is in itself a multi-phase problem and therefore needs a multi-phase model in the software. There are therefore two occurrences where multi-phase physics are needed, the inlet air is humid and will therefore be considered a multi-phase gas containing water molecules, the condensate will form a film as mentioned previously (see section 2.2), and will use the physics called Fluid film (section 3.2.2), this fluid film contains a multi-phase fluid, which will form into ice as the simulation progresses.

As the name suggests Dispersed Multi-phase (DMP) simulates dispersed phases in the Eulerian manner. This type of multi-phase model combines aspects of both the Lagrangian multi-phase and the Eulerian multi-phase. According to Siemens Simcenter guide on DMP [26] it is advantageous to use models such as this when modeling icing applications, as it is not as time-consuming as Lagrangian methods. A coupled solution of background and flow energy is needed in such applications where Eulerian methods do not support this. The disadvantage is that DMP is limited in complexity when it comes to the choice of physics models, some interactions can therefore not be modeled especially complex wall interactions such as splashing.

3.2.2 Fluid Film

Condensate will form in a film manner around the tubes and therefore using a fluid film module in the software will suit the conditions best. This fluid film allows for complex interactions with the surrounding environment. In an icing simulation, the fluid film will be initiated as an infinitesimally small fluid film on top of the tubes. The physics is then adjusted according to the specifications of the problem. The fluid film in this case allows impingement of droplets, which in this case represents the humid air. Gravity is a big factor in ice formation so it is an obvious requirement to let gravity act on the thin film as well as shear forces. The thin film is also allowed to deflect and have droplets exit in case that should happen, see Fig. 10 for a clear picture of how a thin film would look on a tube. The film allows solidification and hence icing.

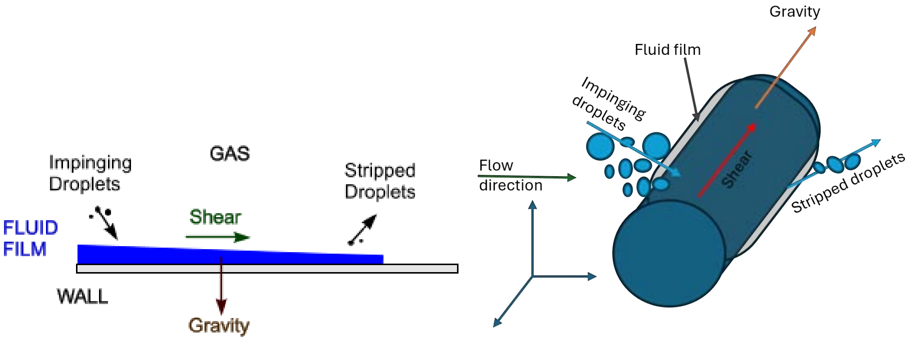

(a) (b)

Fig. 10. (a)Fluid film figure from Sim-center on Fluid film [27]., (b) Fluid film adaptation of fluid film on a tube such as that seen in a heat exchanger.

3.3 Test Rig Setup

The test rig outside the heat exchanger consisted of several essential parts that led to a complete test rig setup, as seen in Fig. 2. The test rig setup was then conducted by choosing corresponding systems according to Section 3.1. This included the cooling unit, pumps, heaters, humidifiers, and auxiliary units such as manifolds, bleeding systems, and the design of the test section assembly itself. This work can be found in the adjacent thesis by Pontus Miltén [28].

3.4 Testing Methodology

This section outlines the testing measurements and instrumentation as well as the intended tests to be carried out. Finally, it includes how an error analysis will be utilized in this project.

3.4.1 Measurements and Instrumation

The test rig consists of several measuring devices to capture the behavior of the HEX and the condensate inside the test section. The rig and the probe locations can be seen demonstrated in Fig. 11 below.

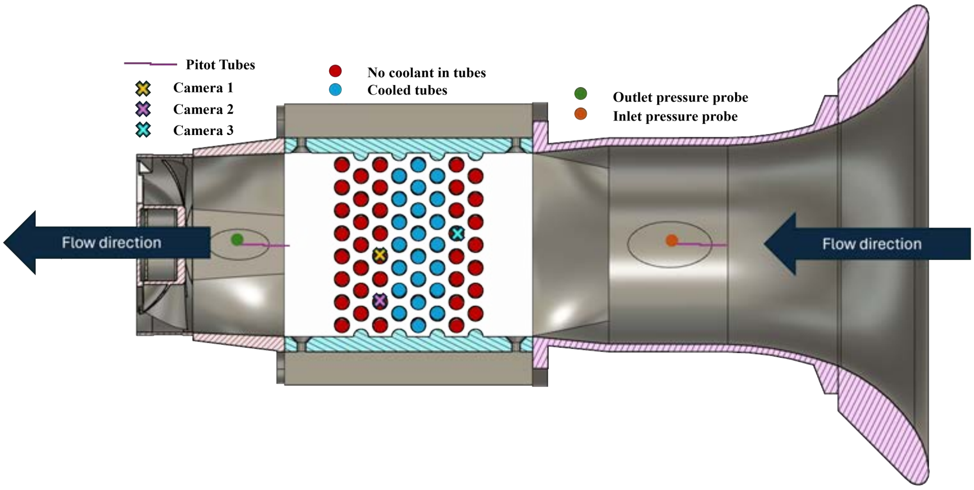

Fig. 11. Schematic showing a cross-section of the rig with markings indicating the instrumentation used for the test.

Temperature Probes

One of the key measurements taken is the temperature of both the air and the coolant in the respective inlet and outlet. The temperature sensors used are thermocouples with a handheld reader that displays the inlet, outlet, and change in temperature. The placement of these sensors is denoted by the green and orange circles in front and behind the test section in Fig 11.

Pitot Tubes

Pitot tubes measure the difference in total and static pressure. These measurements are used primarily to ensure proper flow conditions in the inlet. The addition of a pitot tube behind the test section would also provide the pressure loss across the heat exchanger. The position of the device behind the test section should be taken into careful consideration as it should be placed far enough away from the wake if the pressure drop is the intended measurement.

Cameras

Inspection cameras were used to observe ice accretion on the tubes. They were implemented by inserting them through the holes in the plexiglass and sliding the corresponding tube down, keeping the flow characteristics as true as possible while achieving a good view of the cooled tubes.

Humidity Sensor

The HM1500LF, is the humidity module used for the experiment. This is a capacitive humidity module that outputs a voltage that is used to determine the relative humidity. The manufacturer provides all data in the data sheet (seen in [29]). For this case, the expression for relative humidity is written as follows

$$RH_{actualT} = -1.91E^{-9}V_{out}^3 + 1.33E^{-5}V_{out}^2 + 9.56E^{-3}V_{out} - 2.16E^1 \tag{3.1}$$

and is compensated as stated by the datasheet.

Data Collection

Since this is the early stages of the test rig the data collection of these instrumentation was done by recording all the values using a phone and aligning the recordings as a post-processing step.

3.4.2 Comparison of Heat Transfer Calculations and Test Data

Heat transfer is a crucial aspect to investigate during the freezing process. This will determine how accurately the ϵ-NTU method can predict the temperature change when observing humid air during condensation and freezing. In the calculations from section 3.1 transport properties for air and coolant are assumed. Under the conditions experienced in the rig, the values might differ slightly due to the air's humid nature. To assess the validity of this method the temperature change can be measured and compared to that shown from section 3.1. The comparison will be made at two mass flows on the air side, one slower (denoted by Test 1) and one faster (denoted by Test 2). Where the inlet velocity of Test 1 is around 1.8 m/s and the inlet velocity of Test 2 about 3.2 m/s.

3.4.3 Ice Buildup Comparisons

A main part of the thesis is ice accretion. Investigating the DMP model's ice prediction would provide a deeper understanding of a multiphase heat exchanger. The DMP model, as explained in section 3.2.1, should demonstrate visible solidification which can be compared to the conducted tests. These tests will run at the same two conditions as suggested in the previous section.

3.4.4 Error Analysis

Given that a substantial portion of the gathered data was obtained through self-conducted experiments, performing a thorough and reasonable error analysis is essential. This analysis is based on Taylor's theorem, and the relevant code is appended in appendix G. Various sources of error must be considered, as measuring equipment can occasionally yield misleading readings. The error propagation based on source terms can be identified. The project accounts for potential errors and identifies areas of inaccuracies and their effect on results.

4

Results

This chapter presents the results gathered in this thesis. It includes the characterization of the rig and the conducted tests. Results from numerical analysis will be compared to the physical tests.

4.1 Test rig characteristics

The sizing of the heat exchanger rig introduced limiting factors for dimensions, operating time, and component sizing.

After the calculations shown in appendix A, the size of the heat exchanger was determined to be an 8x8 configuration. This resulted in a run time of approximately 10 minutes before losing too much temperature in the coolant. The bell mouth, fans, and other 3D-printed parts would then be mounted in a plexiglass box, which would artificially create an open-room wind tunnel. To summarize, the dimensions of the HEX section measured [120,165.2,100] mm in [x,y,z] directions, where these directions are seen in Fig. 13. The tubes had an inner diameter,D_{inner}, of 9.5 mm and an outer diameter, D_{outer}, of 10 mm. The resulting shape of the test section can be seen in the ISO-view CAD image in Fig. 12.

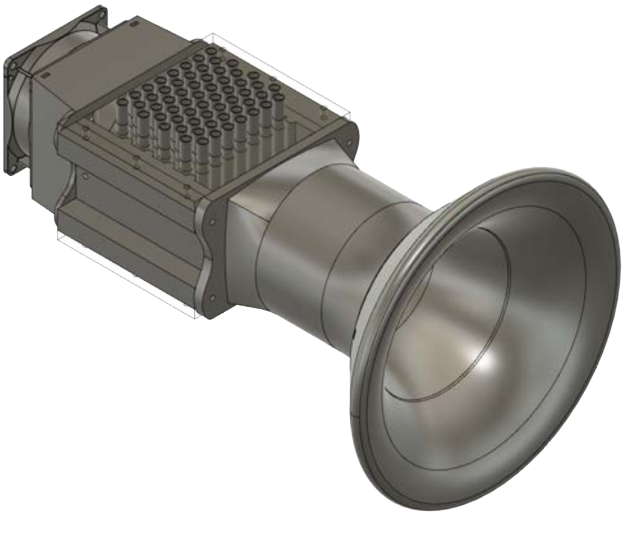

Fig. 12. CAD image of the test section in ISO-view.

For more detailed drawings of the rig see appendix B. The final construction in the plexiglass box can be seen in Fig. 13. The freezer and pump are also pointed out in Fig. 13.

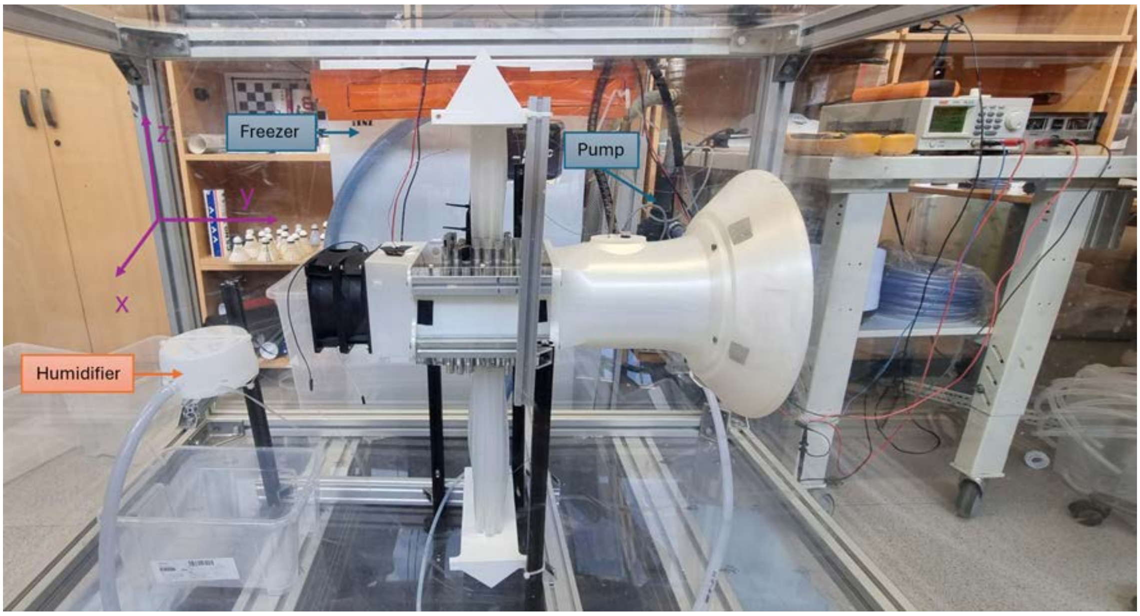

Fig. 13. Final assembled rig inside the Plexiglas's box.

The freezer accommodated 40 liters and could meet the desired temperature of -20 °C. The humidifier produced enough humidity and heat for the first experiments, although more heating could be useful for longer run-time. The pump provided a massflow sufficient to keep the temperature difference across the tubes to less than one degree as desired.

4.2 CFD solution

The initial iteration of the CFD model can be explored in this section. Here the results of reasonable arbitrary conditions are displayed. In both the symmetric and full-scale models ice propagation was visible. The model predicted peaks appearing at the leading edge of the cooled tubes. The inlet conditions for this case stated in Tab. III, where a 5 m/s inlet velocity with an inlet area of 0.0025 m^2, would achieve a mass flow of 0.01525 kg/s. Although this is a section of the entire domain, in reality, this would result in 8 sections as large side by side.

This resulted in the following ice propagation, where the ice function displays ice thickness in millimeters (mm), as seen in Fig. 14 and 15. The ice thickness is set to propagate 20 times faster, therefore the displayed solution time is 20 times slower than the actual time.

TABLE III
CONDITIONS OF CFD ANALYSIS

Velocity inlet (m/s)	Mass fraction [H2O,Air]	Relative Humidity %	Temperature [inlet, tube]
5	[0.2,0.8]	(above) 100 (Saturated)	[50,-20]°C

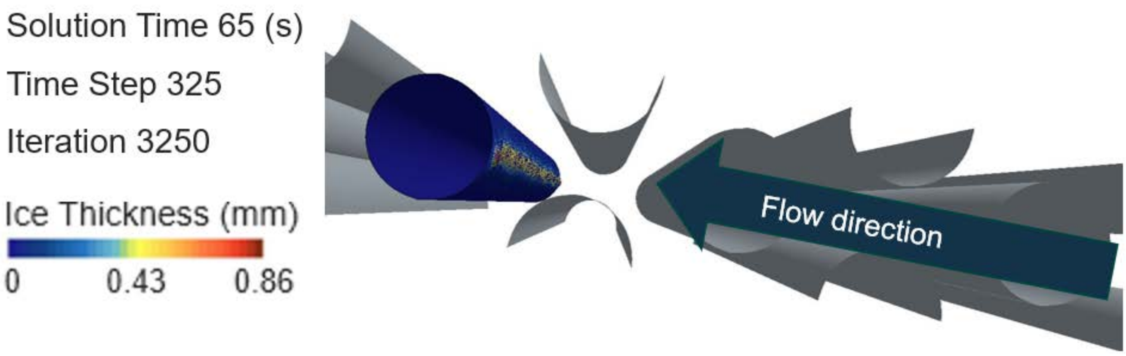

Fig. 14. Symmetric domain with ice thickness displayed.

As can be seen in the figure above after 1300 seconds ice thickness reached its peak of 0.86 mm. Whereas for the full domain in the figure below the maximum ice thickness reached 3.8 mm in only 412 seconds.

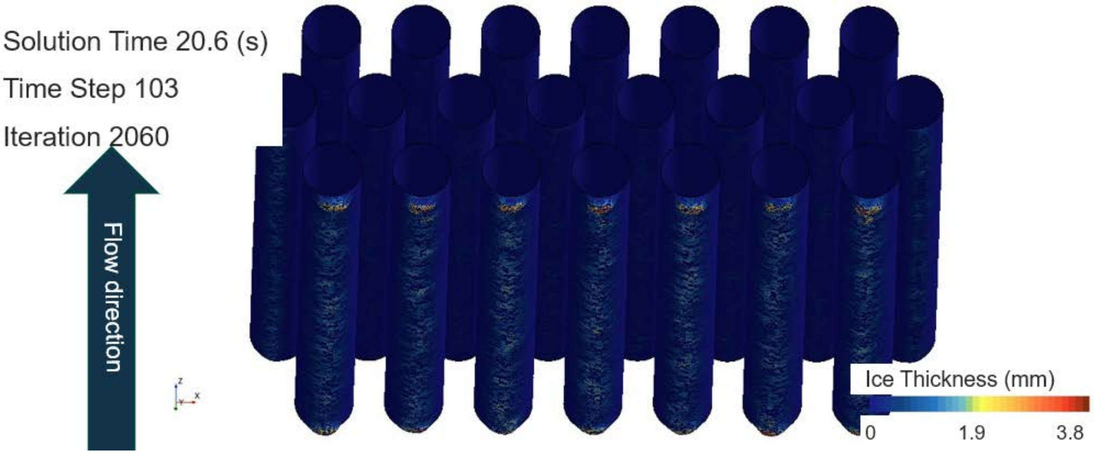

Fig. 15. Full domain (as in experiments) with ice thickness displayed.

Although not displayed at the same simulation time, the full domain in Fig. 15 gathers significantly more ice formation than in Fig. 14, as Fig. 14 is a symmetric domain rather than a periodic. However, as the full domain considers a larger area a larger mass flow can be seen through the domain. This larger mass flow is about 0.12 kg/s instead of 0.015 kg/s in the first case. They both predict most of the ice formation on the leading edge. The full domain (Fig. 15) with three cooled rows also does not show more ice build-up in the rows further back.

4.3 Comparing sizing code heat transfer calculations to tests

The final rig setup consisted of only three cooled rows as mounting all 60 tubes proved to be challenging [28] (seen in Fig 11). This arrangement provided a clear view of the cooled tubes. The sizing code (Appendix C) was adjusted for the corresponding number of tubes cooling the system and resulted in temperature drops seen in Fig. 16.

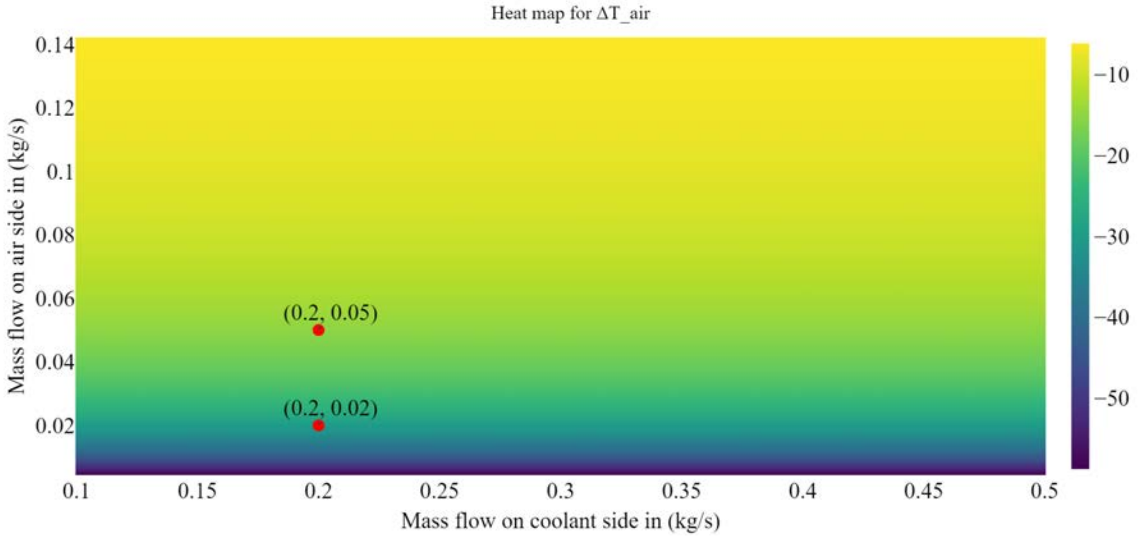

Fig. 16. Color map depicting the change in air temperature with three tube rows cooling the flow. The markings also indicate where the experiments were carried out.

It can be observed that the temperature drop varies slightly from Fig 8. This variation is expected since fewer tubes are cooled. However, the results from the rig tests summarized in Tab. IV, show a larger discrepancy.

For clarification, in the last column of Tab. 17 ΔT shows the inlet temperature change from start of the experiment to the end of the experiment. For Test 1, the slower inlet velocity, the temperature decreased by 16 $°C$ from the start of the experiment to the end of it. Fig. 16 and Tab. IV indicate that the measured temperature on the air side was 77% smaller than expected when compared to the calculations. Test 2 was closer to the expected temperature loss and was 55% smaller. A rather large error in the measurement is suspected due to both cases showing similar ΔT. This will be shown in section 4.5 and discussed further in the next chapter. On the

TABLE IV
CHANGE IN AIR TEMPERATURE MEASURED IN EXPERIMENTS

Test	$\Delta T_{air(experimental)}$ °C	$\Delta T_{air(analytical)}$ °C	ΔT_{air}°C **from start to end of test (in seconds)**
Test 1	-7	-30.4	16 (550s)
Test 2	-7	-15.4	8.7 (245s)

other hand, the calculations for the coolant side showed promising results.

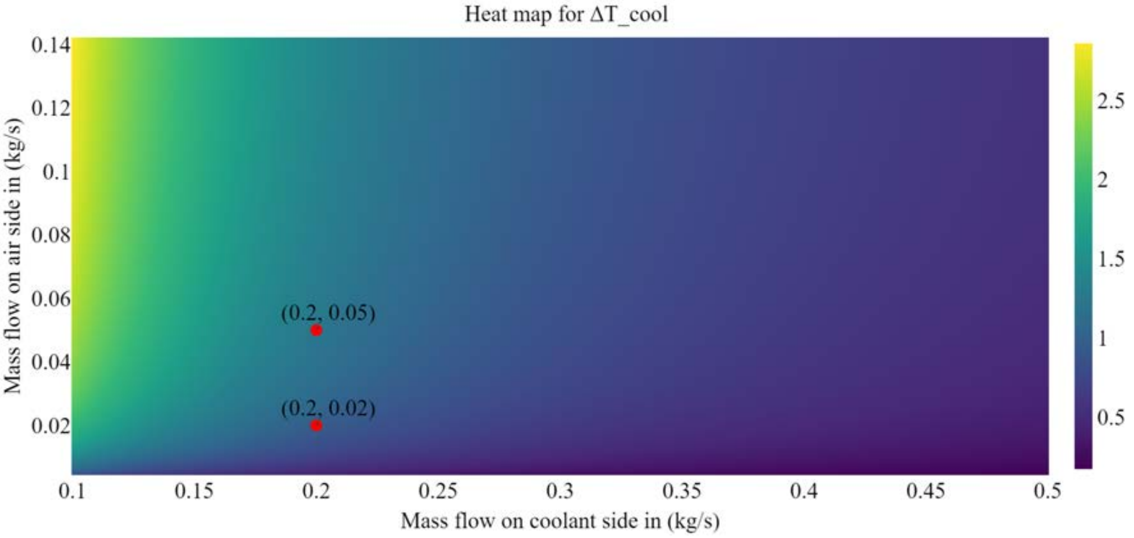

Fig. 17. Color map depicting the change in coolant temperature with three tube rows cooling the flow. The markings also indicate where the tests were carried out.

As the rig was dimensioned to achieve a ΔT_{cool} below or close to one degree it was expected to meet these requirements. The massflow on the coolant side is therefore not measured but it can be seen that the heat transfer does not vary significantly after 0.2 kg/s. Therefore it can be assumed that this massflow is achieved and since both ΔT measure close to one degree the massflow would not affect the results. Both tests showed close to the expected results and are summarized in Tab. V.

This means the expected temperature differs by less than one degree in Test 2, where the largest difference is observed. The accuracy in this case can be said to be too big, the measurements are not accurate enough. As per the air temperature measurements, this will be brought up in further detail in the coming sections.

TABLE V

Change in coolant temperature measured in experiments

Test	$\Delta T_{cool(experimental)}$ °C	$\Delta T_{cool(analytical)}$ °C	ΔT_{cool}°C **from start to end of test (in seconds)**
Test 1	<1	0.9	5 (550s)
Test 2	1-1.5	1.2	5 (245s)

4.4 Comparison of ice propagation in CFD to experimental data

This section presents the ice accretion results observed in the experimental investigation and compares the identical CFD scenario. The first subsection will explore the slower airspeed, while the subsequent section will show the faster airspeed. Raw data for both experiments are seen in appendix E and a zip file is provided for all the results in appendix F.

4.4.1 First Test: Slower Velocity Inlet

The initial conditions of this case are seen in Tab. VI

TABLE VI

Inlet conditions of slower airflow test

Dynamic Pressure (Pa)	**Velocity (m/s)**	$T1_{air}$°C	$T1_{cool}$°C	**Relative humidity in%**
2	1.8	45	-10	35

The results can then be shown as snapshots in time, where the views observed in the experiments were replicated in CFD. The starting point of the experiment can be seen in Fig. 36- 38 in appendix F. It can be observed that only condensation has started. Most condensation can be seen on the frontmost row of cooled tubes in Fig. 38 appendix F, where big droplets are observed. A layer or a “fluid film” can be seen forming in the experiment in Fig. 18, with a red circle explicitly indicating the tube with a condensate film. The arrow shows droplets that have disturbed the film. The CFD solution in Fig. 36 - 38 (b) (in appendix F) shows small indentations where it predicts ice to form, the size is still insignificant. The comparison between the figures from CFD and experimental figures shows that CFD is already at this time interval predicting ice formation.

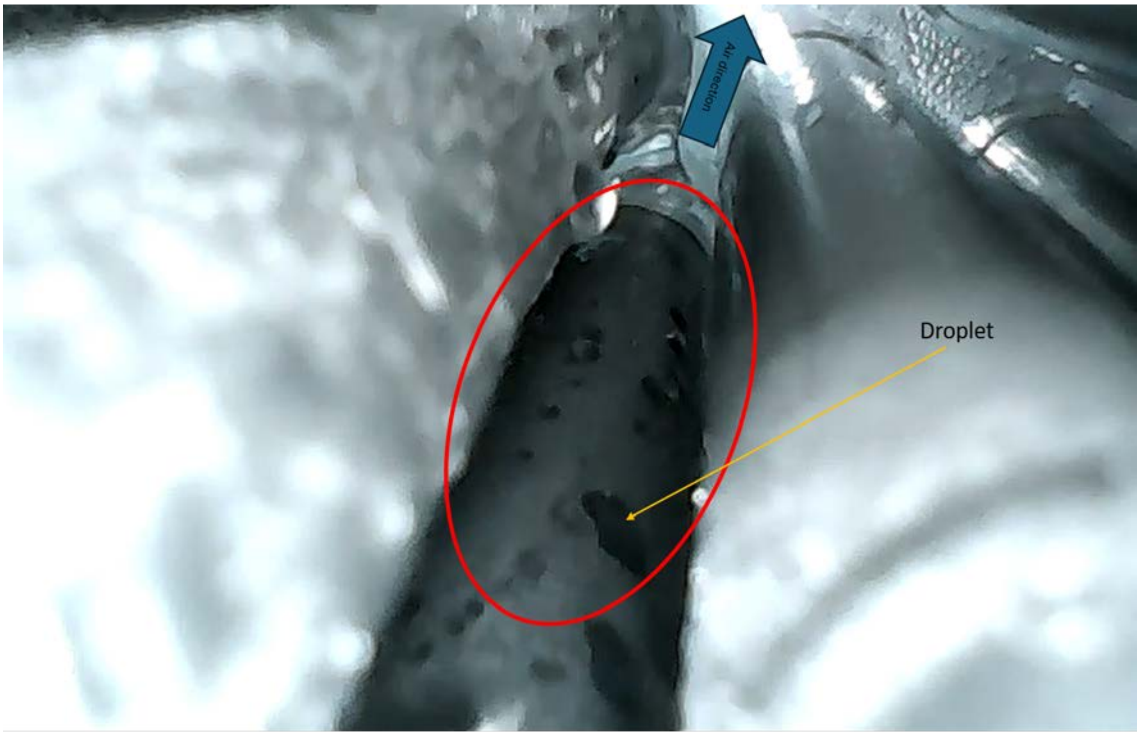

Fig. 18. Image depicting snapshot at the start of the experiment (20s) from camera 1 with the circle indicating a visible fluid film.

Frost can be observed 40 seconds into the experiment from camera 1. The frost described can be seen in Fig. 39 - 41 in appendix F. Clear ice propagation from the bottom of the tube in Fig. 19 can be observed and circled for clarity. This occurs at about 70 seconds into the experiment and is most visible from camera 1, the rest of the cameras can be seen in Fig. 42 - 44 in appendix F.

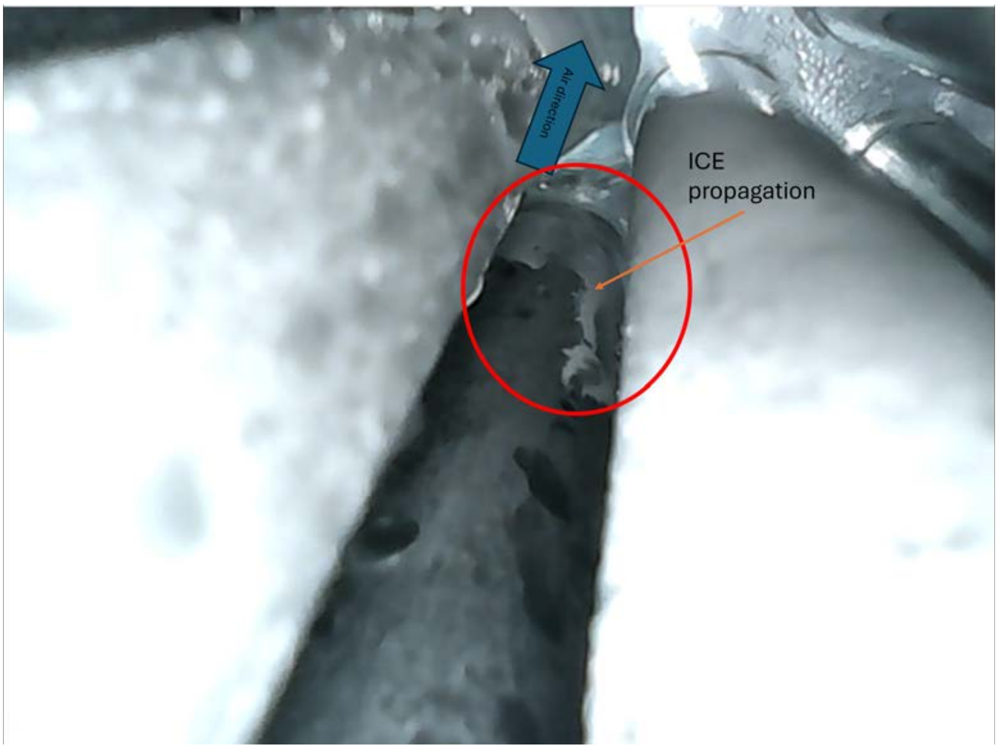

Fig. 19. Image depicting snapshot at ≈ 71 seconds into the experiment from camera 1 with the circle indicating an ice propagating vein.

Ice could then be seen building up, reaching somewhat of an equilibrium with the condensate dripping down the tube melting some ice. This equilibrium state can be shown in the next set of images in Fig. 45 - 47 in appendix F. The line of ice accretion is pointed out as per usual in Fig. 20 - 22.

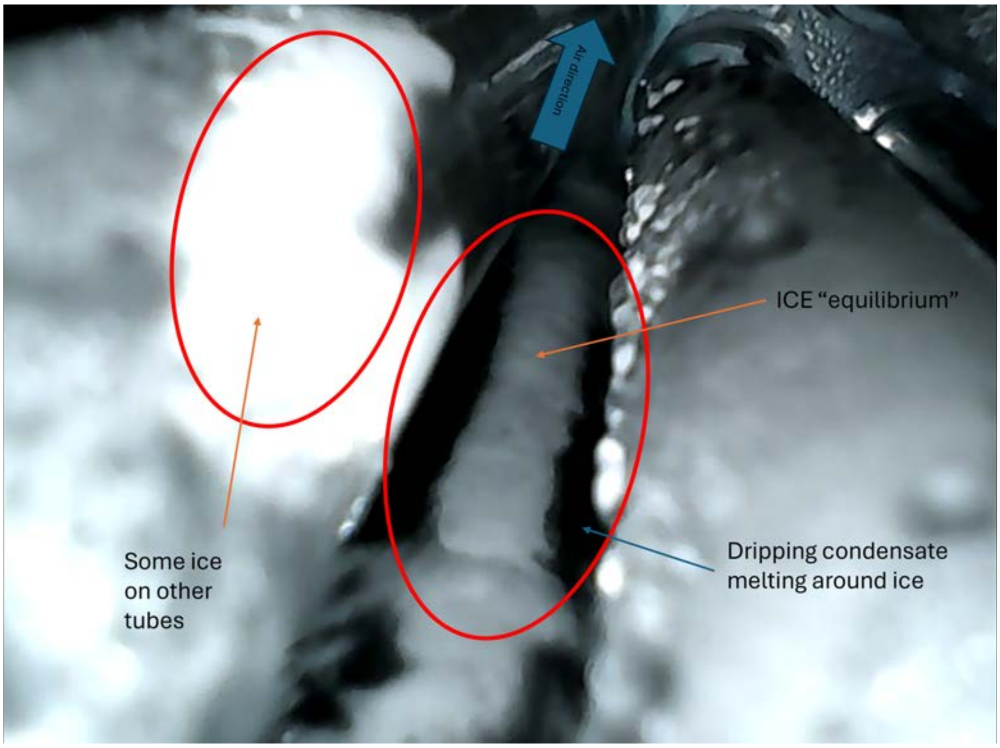

Fig. 20. (a) Camera 1 at ≈470 seconds into the experiment indicating types of ice build-up.

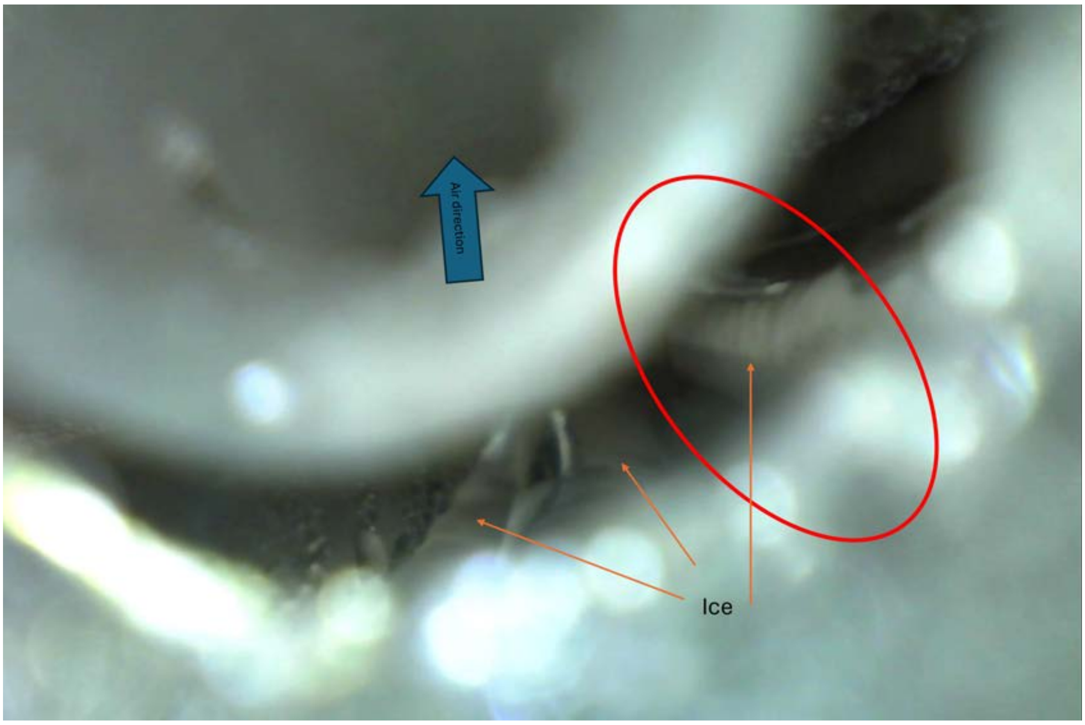

Fig. 21. Camera 2 at ≈470 seconds into the experiment indicating types of ice build-up.

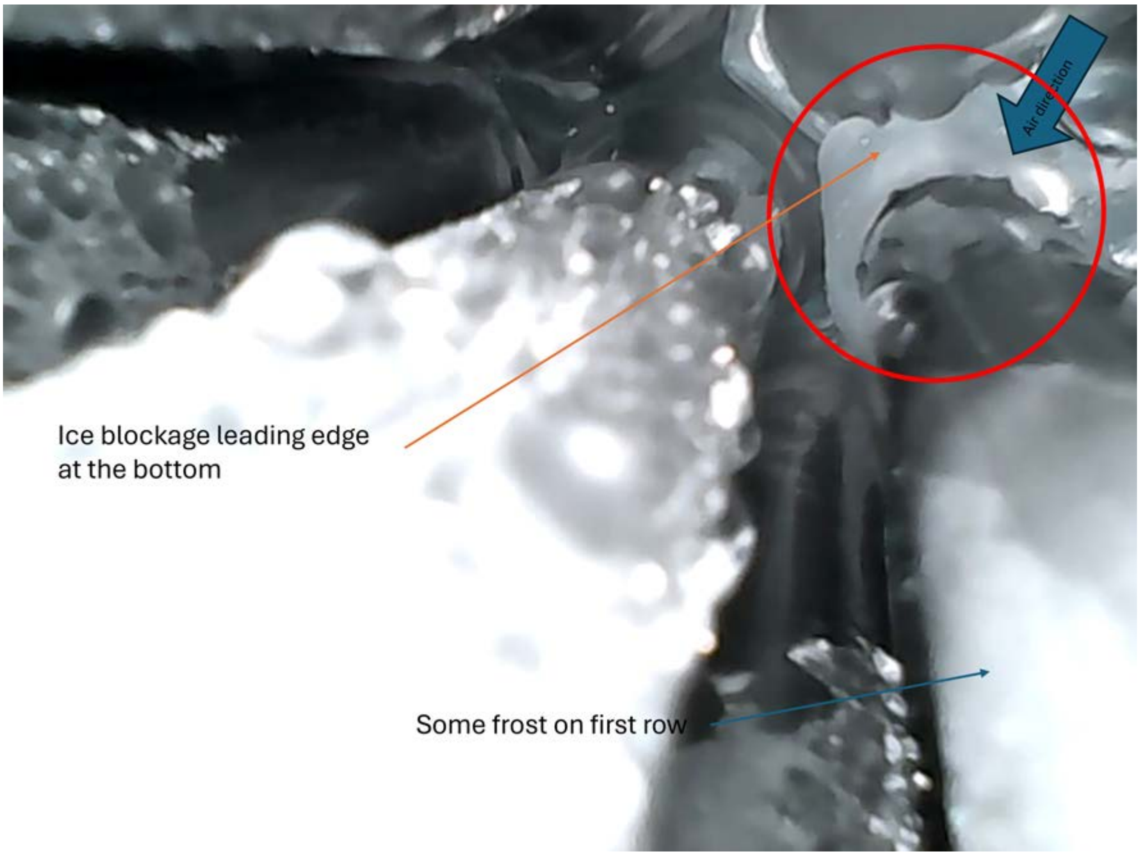

Fig. 22. Camera 3 at ≈470 seconds into the experiment indicating ice build-up.

Towards the end of the experiment, the total ice layer is seen in the last row of tubes through cameras 1 and 2 in Fig. 23. Some ice propagation could also be seen at the leading edge of the second cooled row observed in Fig. 24. The comparison to the respective CFD view is seen in Fig. 48 - 50 as per usual in appendix F.

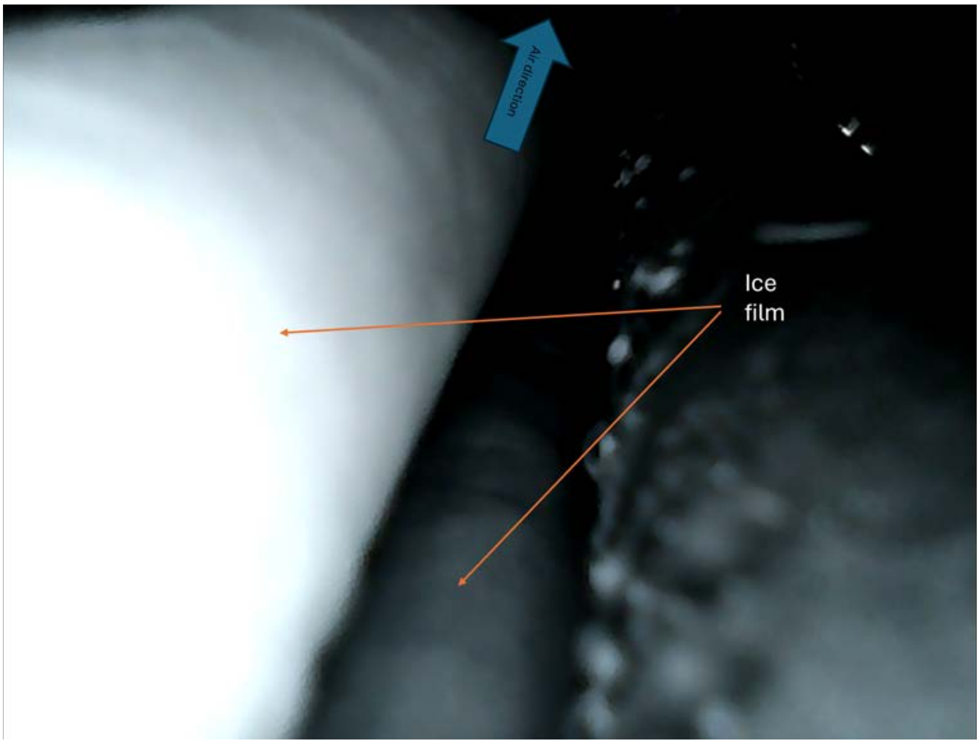

Fig. 23. Camera 1 at ≈507 seconds into the experiment with a thick ice film.

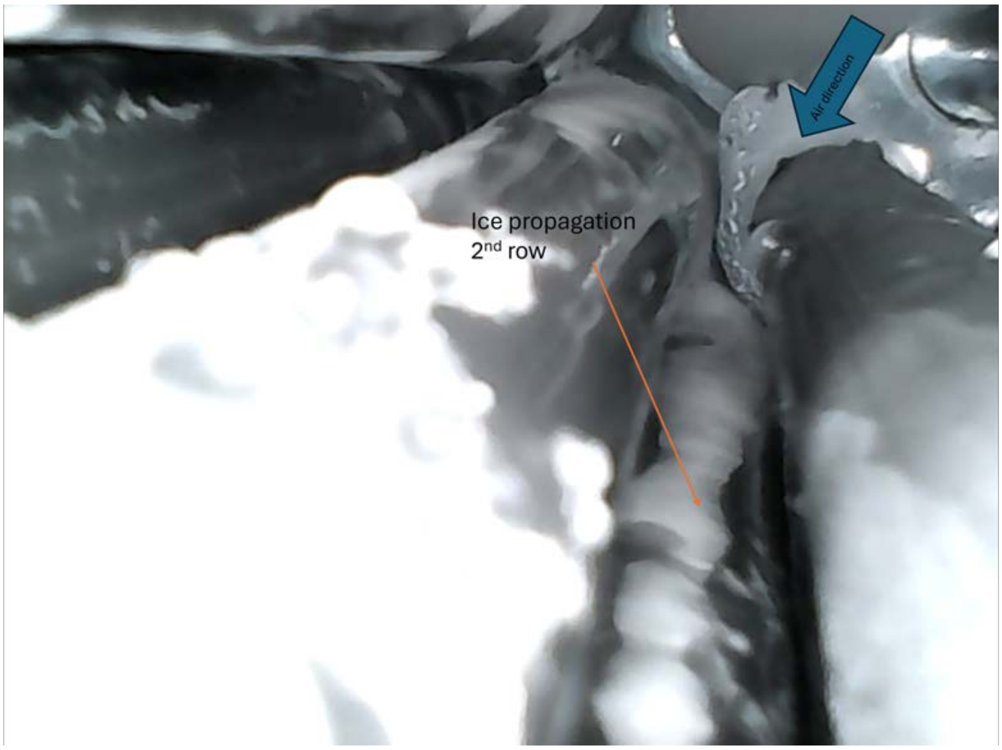

Fig. 24. Camera 3 at ≈507 seconds into the experiment with a propagating ice vein on the second cooled row.

A final image of the complete domain represented in CFD in Fig. 25 for a clear comparison to the test. The CFD predicted most ice thickness at the leading edge of the first row whereas in the experiments the opposite occurred. The last row froze first then the second, even though the bottom of the first row's leading edge ice could be seen blocking the spacing. Another remark is that the film in CFD is never seen completely frozen as in Fig. 23. The numerical simulation seems always to increase peak ice formation.

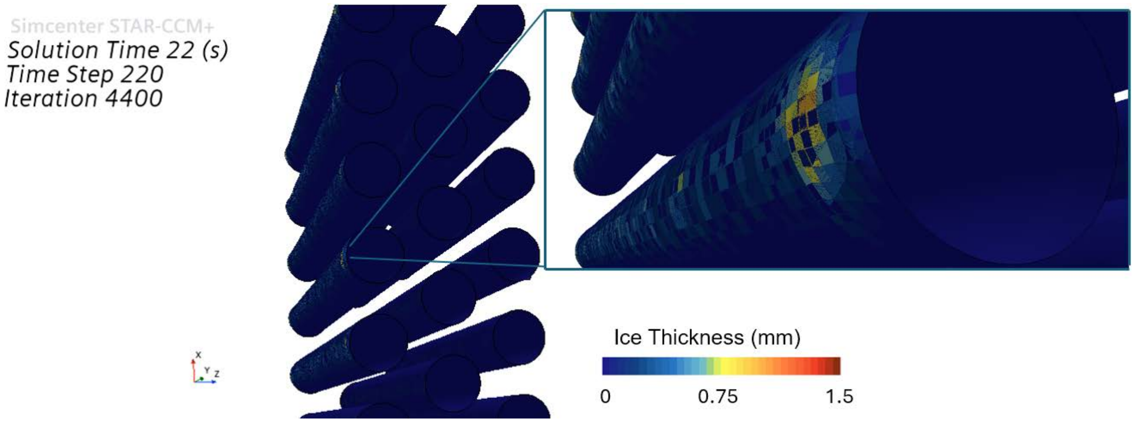

Fig. 25. CFD showing total ice thickness of entire domain.

Fig. 25 shows majority of ice formation on the top and bottom of the tube, near the wall, with the maximum thickness observed as roughly 1.2 mm.

4.4.2 Second Test: Faster Velocity Inlet

The initial conditions of this case are seen in Tab. VII

TABLE VII

INITIAL CONDITIONS OF SLOWER AIRFLOW TEST

Pitot Pressure (Pa)	**Inlet Velocity (m/s)**	$T1_{air}°C$	$T1_{cool}°C$	**Relative humidity in%**
6	3.2	45	-10	60

As can instantly be noted, the relative humidity on this day was significantly higher than on the day of the first test. The resulting test is then seen in similar photos where the observed experiment was replicated in CFD. It is worth noting that the fans malfunctioned during the middle of this test resulting in a shorter test. The start of the experiment can be seen in images from Fig. 51 - 53 in appendix F. As can be seen in the previous section initial condensation is observed, this is seen in Fig. 26.

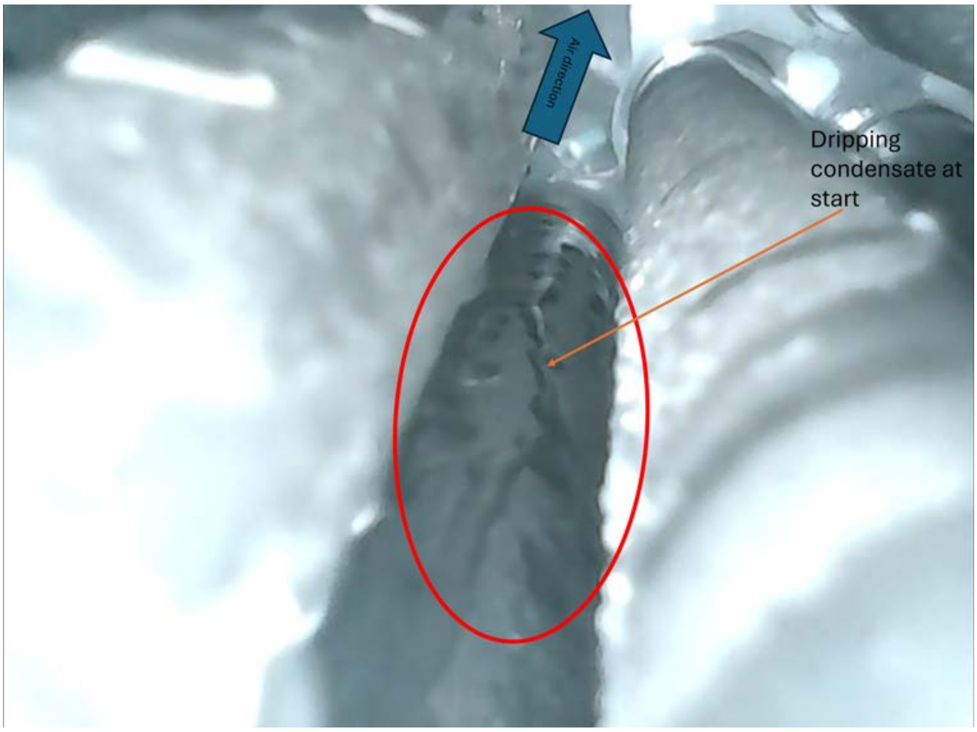

Fig. 26. Image showcasing more condensate than observed in slow airspeed test.

As time passes, more condensation is observed on the tubes but no frost or ice is built. Condensate can be seen flying through the HEX in the recordings and after roughly 100 seconds the temperature drop was deemed too extreme for comparison. As mentioned one of the fans also malfunctioned and the test was consequently cut short. The observed tubes at the end of the experiment can be seen in Fig. 54 - 56 in appendix F. Nonetheless, with close inspection, more condensate droplets are visible especially when observing camera 3 and the leading edge of the first row in Fig. 27.

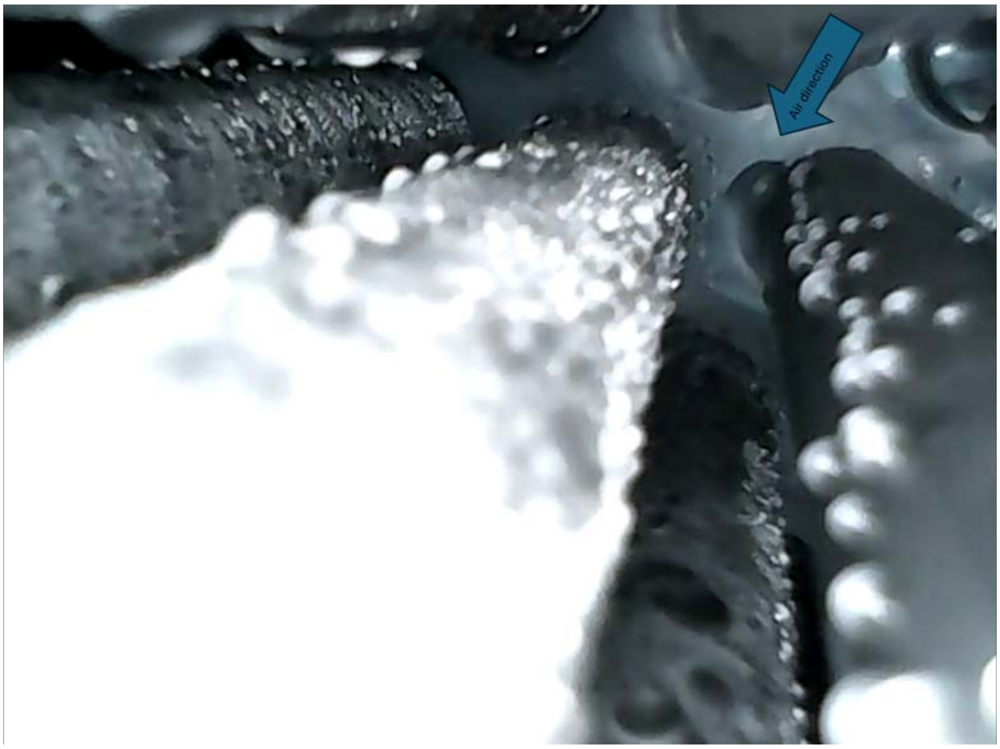

Fig. 27. Image showcasing more condensate droplets on the leading edge.

On the other hand, the observed ice accretion in the CFD file is significant and indicates ice thickness of 0.7mm at 130 seconds as seen in Fig. 28. This is noted to be less than in Fig. 25 where the simulation has run longer. Whereas if compared at the same time the second test in CFD can be seen at the same solution time in Fig. 29. In Fig. 29 ice thickness is observed to be 2.2 mm at its thickest.

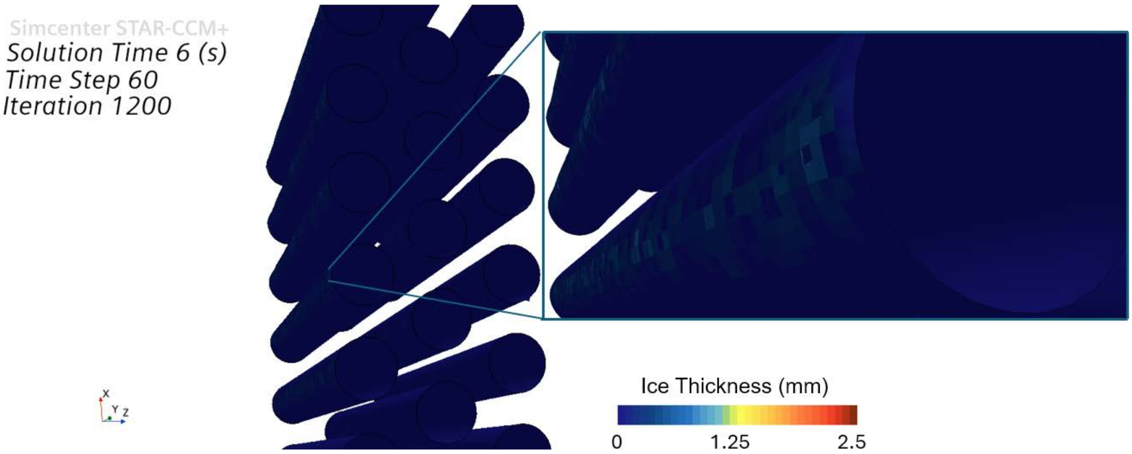

Fig. 28. Total ice thickness in CFD simulation at 130s.

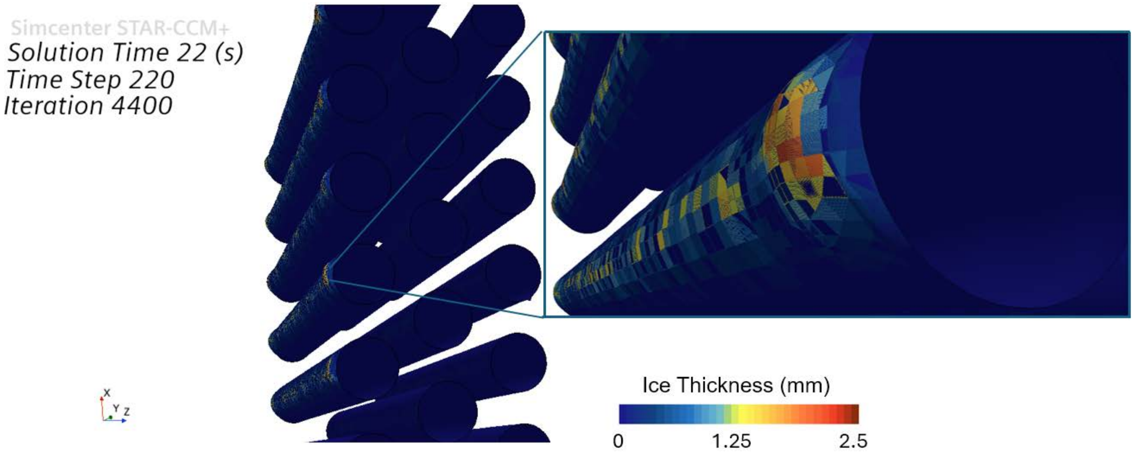

Fig. 29. Total ice thickness in CFD simulation at 440s.

Where the majority of the ice, similar to Test 1, is predicted on the top and bottom of the tube. The maximum ice thickness achieved here is about 2.5 mm.

4.5 Error Analysis

As evident from the results in section 4.3 and the tests in section 4.4 the important error source was the temperature or rather the resulting temperature measurement. As a result, a deep investigation into the temperature error is examined in this project.

From a numerical standpoint the change in temperature, described in eq. 2.15, depends on several other variables. A dependency tree can be seen in Fig. 30

Fig. 30. Figure demonstrating possible error sources within temperature drop (on air side as an example).

As can be seen in the figure, ϵ relies on several factors which also rely on other factors hence a domino effect of error can occur. As seen in Tab. VIII, the error result was broken down into pieces.

Error percentages, considering reasonable absolute errors as seen in Tab. IX(can also be seen in detail in appendix I Fig. 59). In the detailed table, it is seen that values for errors are chosen for each possible source. The assumed absolute error stems from manufacturing error in values such as D_o and D_i, whereas for values such as h_{air}, h_{cool}, and c_p educated guesses on the possible error were made. However the

TABLE VIII
Summed up error breakdown in an analytical case.

Value	**Uncertainty %**
ϵ	16.37
$C_{min,air}$	1.22
$T1_{cool}$	15
$T1_{air}$	3.33
ΔT_{air}	19.91

TABLE IX
Assumed absolute error.

Value	**Assumed error**	**Test error**
h_{air}	50	-
D_o	0.1	-
D_i	0.1	-
k_w	20	-
h_{cool}	5	-
$c_{p,airl}$	5	-
$\dot{m}_{air}$	0.05	-
$T1_{air}$	1.5	2
$T1_{cool}$	1.5	9.5

assumed error on values such as $T1_{air}$ and $T2_{air}$ where given by the manufacturer. In the column labeled Test error, the observed error in the test is stated.

In reality, during the tests, it was discovered that the thermocouples measuring the coolant temperature seemed to vary compared to a normal household thermometer by a significant amount (about 5-8 $°C$). This resulted in an error of 90% in the temperature measurement of the cooled inlet when comparing the thermocouple to the household thermometer. Considering this error as an uncertainty in the code, changed the overall uncertainty of the numerical calculation in temperature of the air to about 24.3% compared to the previous 20% in Tab. VIII. The uncertainty within the calculation is also a result of the code and can be seen in the bar graph in Fig. 31. This is named the inflicted error as it scales how each variable affects the calculation of ΔT_{air} in the case of a larger thermocouple error.

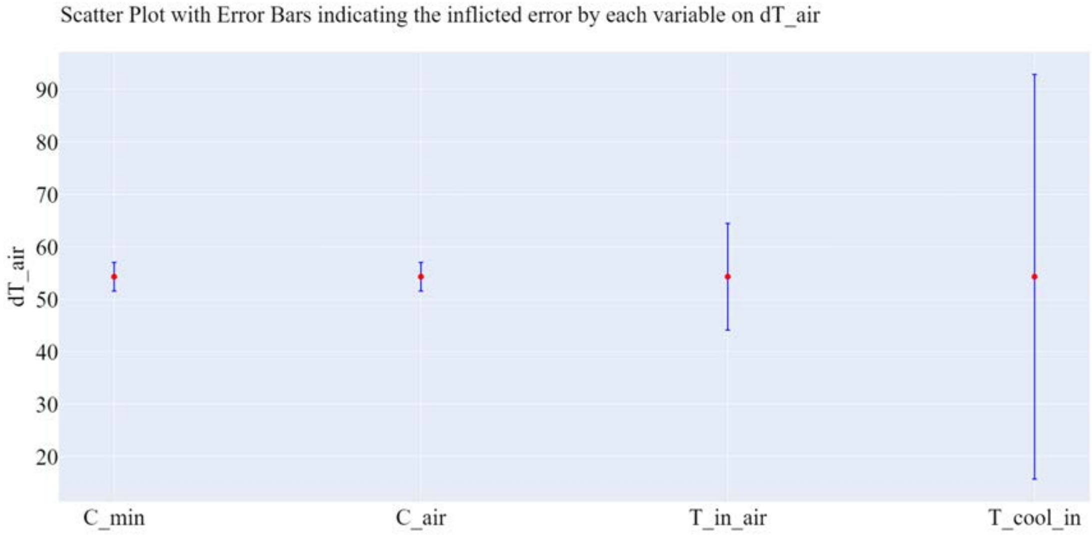

Fig. 31. Inflicted error of each variable on ΔT_{air} in the second case.

It should be clarified that the error bar in the could not physically produce a higher ΔT than seen in the red dot. Another error source can be seen in the pitot tube measurement, as the handheld devices during the tests showed only a single digit of accuracy, which would result in a larger margin of error. Other sources of inaccuracies can be found in the relative humidity probe, where the manufacturer provides an error margin of the displayed measurements [29].

5

Discussion

In this chapter, the highlighted results are dissected by examining them closely and discussing them in detail. The validity of the results is shown, and their implications are made clear. The chapter will address topics such as the sizing calculations, the numerical solution, and the test results

5.1 Heat exchanger rig

The heat exchanger in this project uses a standard compact HEX, to facilitate faster prototyping of the rig. Sizing the rig with pressure and temperature changes proved beneficial as it provided a simple script based on correlations that sized the rest of the components accordingly. The pressure losses in the coolant system were simpler to deal with, however, the difficulty occurred when finding a high-quality pump that tolerated the cold temperature. The rig was able to achieve the operating range desired for the project, but in cases were a higher Reynolds number is desired, bigger fans are needed. The rig inlet provided stable inlet conditions as it should, but the outlet pitot tube integration was not optimally implemented as the tube ended up in the wake of a tube preventing pressure loss validations.

The temperature change provided good dimensioning criteria on both the air and coolant side. On the coolant side, a reasonable freezer was selected to provide the volume of coolant needed for keeping the temperature of the liquid at the desired temperature for the desired time. However, if the test time is to be extended a larger cooler would always be beneficial. With the hand calculations made in appendix A the 40 liters of coolant would serve approximately 300s if all tubes were cooled, before changing drastically in bulk temperature. On the air side, the fans were just sufficient to achieve the desired flow conditions. The heat source, provided solely through the humidifier, was insufficient to maintain constant inlet temperature on the air side while running the rig. This made temperature control challenging, therefore, controlling the humidity was also difficult.

5.2 Numerical Investigations

This section will discuss the numerical analysis, including the results illustrated in images such as Fig. 16. The comparison to the test results will be discussed in accordance with the numerical side. The CFD model and solution will also be discussed in detail.

5.2.1 Heat Transfer Calculations

The temperature drop is displayed in the color maps in section 3.1, indicating that the air temperature drop is weakly dependent on the mass flow on the coolant side, unless for very low mass flows. The critical criterion on the air side is the air mass flow. However, as seen in later sections these calculations show discrepancies when compared in the adjusted color maps in section 4.3. This can be due to the assumptions made, of which some are more reasonable than others.

The assumption of a constant thermal conductivity, k, in the air and on the wall in cases of multiphase HEX cannot be valid during the ϵ-NTU script. In the tests the air is rather humid as per requirements, however, in the ϵ-NTU calculations, no consideration of the air humidity effect on heat transfer was considered. Neither the consideration of droplets on the tube walls nor how ice affects this heat transfer. Adjusting the ϵ-NTU method to accommodate time-varying wall heat transfer would result in more accurate calculations.

As the error analysis in section 4.5 suggests, the measuring devices also presented inaccuracies. When comparing numerical analysis to tests this can seem like large mismatches but with an error analysis, these sources can be broken down. It was therefore discovered in the experiments that the thermocouple on the coolant side showed a significant difference, this could therefore also be the case for the air thermocouples, although more unlikely to show such a large discrepancy here. As thermocouples also utilize current to measure temperature the humid air could potentially be a disturbing factor although very unlikely.

5.2.2 CFD Solution

The CFD considered constant temperature on the tubes that did not change with ice buildup. The mesh morphed to accommodate new prism layers and avoid zero-volume cells. The morphing of the mesh did not adopt a new heat transfer gradient but considered the outer layer of ice also a constant temperature of -10 °C, which in reality is not the case. Enforcing a temperature where the highest heat transfer from the air exists (leading edge of tubes) is not accurate. By utilizing one of the other two boundary conditions mentioned in section 2.3.1 the heat transfer can be modeled with higher accuracy. The boundary condition of choice would be to model the fluid inside the tube resulting in the highest similarity.

The CFD considered all the tubes as one shell region with one thin film, which has not been further investigated if one region per tube would make a difference. The CFD did not consider condensation on the top and bottom surfaces, but in experiments, these proved to condensate considerably more than 3D-printed plastic which could have influenced the results.

After an initial investigation of the CFD setup, the DMP model seems to predict icing on the leading edge of tubes, and in the case of the full domain, more icing on the first row. At a glance, this could seem reasonable, as the air stagnates here. This also aligns itself with the ice accretion on wing element as explained by the theory in section 2.2.2. Still, this is not expected to be the case in reality, as compared to the airfoil case, the HEX experiences hot humid air and cold surface rather than the other way around. As seen by the test results the observed ice is formed in the last row as the literature supports in [9]. The mentioned “cold corner” in this case refers to the last row of tubes. In reality, the first row collects most of the condensate. Due to gravity this condensate only freezes where it is pooled up, in this case, the bottom surface.

The CFD is set up with the recommended settings by Simcenter and therefore no investigation into adjusting the modules was made which could be a source of error in the validity of the simulations. Multiphase solvers are heavily dependent on the solver settings and are very case-specific. With a more thorough investigation into the CFD solvers, the ice propagation could potentially be resolved properly. Adding boundary layers that somehow take into consideration condensation on different surfaces and implementing surface tension could also be an interesting addition to the CFD setup. Finally investigating the particle size in the DMP settings should have been done as the observed droplets in the experiments were rather large and would significantly alter the results if modeled accurately.

5.3 Test Results

The test rig provided room for successful tests that resulted in useful data. This section will discuss the data gathered from the experimental investigation in detail.

5.3.1 First Test: Slower Velocity Inlet

In the first test with slower airspeed, clear ice formation could be observed. Ice propagation started from the last cooled row moving forwards in the HEX. A downside of such a compact heat exchanger was displayed in the difficulty of camera placement due to densely packed tubes. This resulted in angles that only allowed observation of the leading edge of the first row and the trailing edge of the last row, lacking the leading edge of the middle row. Nevertheless, ice accretion reached an equilibrium, with a visible strand of icing for a considerable amount of time until it completely covered the tube with ice by the end of the experiment. The test also provided that for these input values, a heat exchanger of these characteristics can freeze. This correlates with the heat transfer calculations indicating that lower air mass flows result in greater temperature drop.

5.3.2 Second Test: Faster Velocity Inlet

In the second test with faster airspeed, no ice was observed. As previously mentioned, a higher relative humidity was achievable on this day which should be considered while discussing the produced results. Under the experiment one of the fans malfunctioned, likely due to the high humidity, which also rendered a small part of the data not useful. Despite these changes, the test continued and no ice could be seen. One observation made throughout the experiment, both the air and the coolant temperature dropped significantly faster than in the first experiment. This suggests that more heat, on the air side, and more cooling, on the coolant side, is needed to sustain these criteria. It also proposes that more heat transfer is occurring, in correspondence to the ϵ-NTU method. Finally, as the speed was higher and no ice was observed, it could be said that more condensate traveled around the tubes of the HEX. This could be due to the higher humidity but also the faster speed and a more turbulent flow regime.

5.3.3 Final Remarks on the Test Regimes

Final comments regarding the regimes observed in the test can be made here. As described in section 2.2.1, condensate in a cascade of tubes can be described as a film or as droplets. In the experiments, before turning the fans on a film of condensate could be observed with occasional droplets running down the tube. However for both test cases as soon as the fans were powered the condensate no longer behaved as a film and rather droplets flying through the HEX. In the CFD model, one of the assumptions made is that the thin film is laminar, one consideration can be to use a turbulent model instead, as that would be more probable given the observed behavior. Using different solvers and investigating how to better utilize the Lagrangian models, implemented in DMP for particle tracking the condensate could be another interesting investigation. This would include an investigation if solely relying on a Lagrangian solver would estimate better results. This would result in not considering the condensate as a film but rather as particles, which could be relevant as the observed condensation droplets were large.

6

Conclusion

This chapter marks the conclusion of the thesis report by considering the rig design and the rig performance. Finally, suggestions for improvements on the rig and the importance of investigation into multiphase HEX numerically and physically are covered.

6.1 Heat Exchanger Rig Sizing

As the sizing of the rig produced a functional heat exchanger rig, the primary goal of the thesis was achieved. The sizing provided a way to dimension and set the criteria fast. Pressure losses were deemed significant and careful design consideration should be accounted for. The rig was intuitive to start up and use for repetitive experiments. Overall the rig used a good design but lacked some specific aspects that could be revised in future work.

6.2 Numerical Investigation of a HEX

Heat transfer estimations are inherently difficult, especially when dealing with multiphase exchangers. Assuming dry conditions as a first guess turned out to be a reasonable choice, however, a section should have been added considering humidity and condensation.

On the other hand, the CFD setup did not result in similar results to the experiments but offered a deeper understanding of the underlying difficulties. It became evident that multiphase models are sensitive to application cases. The DMP model coupled with a shell region thin film works well for the icing of airfoils on the wings of planes or even the nacelles of the engine with the recommended settings. The model is validated for such a case and, therefore very applicable for external aerodynamic devices on an aircraft. The model still predicts ice accretion on the leading edge on the frontmost row which is not the case in heat exchangers. This indicates the model is heavily dictated by the speed of the particle of humid air and their interaction with the first element assigned a film region that they come in contact with. However, ice accretion in a heat exchanger is more complex than that and would require a specific set of settings to accommodate this.

The conclusion on whether a multiphase solver such as DMP is an optimal choice cannot be definitively drawn from this project alone. However, the module should certainly be investigated further in multiphase heat exchangers.

6.3 Experimental Investigation of Ice Accretion

In complex problems such as heat transfer, well-designed experiments are the key for understanding, ice accretion in a cryogenic heat exchanger, this is no different. The results gathered in the experiments conducted are highly valuable even though they may not be optimal. These results provided a good initial understanding of experimental ice formation and numerical estimations. With some reconsideration that will be mentioned in section 6.4 the results from the test could be better compared to the numerical results. It can be seen in extreme cases that blockage can become an issue, but luckily this is only in slow-moving air, or after shutting off the rig. This indicates that as long as the temperature is high enough and the air speed is high enough ice buildup would not propagate from the tube due to the residual energy in the air. This residual energy can be seen as both the heat in the droplets in the humid air, but also the energy within the flow meaning the condensate flying around and melting any ice before it has time to propagate.

When sizing a heat exchanger, design considerations are important. Gravity has been observed to significantly influence ice buildup, although this may change with higher air velocities. Therefore, airspeed can be considered a critical factor in ice formation. Ice tends to propagate from areas where colder air temperatures can be found. The heat exchanger could be strategically designed to allow non-critical ice buildup in certain regions. This would change the pressure drop resulting in a different heat transfer coefficient and hence a different effectiveness. An educated guess would say that the effectiveness of the HEX would worsen. However, as not enough ice is observed in the experiments, this would not be deemed critical. Another suggestion could be to ensure that the air never gets too cold by injecting more humid air later into the HEX.

However important insight was gained when comparing the tests to their numerical solution. Not enough information can be found on multiphase heat transfer occurrences. Therefore investigation into solvers and models that can better resolve the heat transfer process under heavy condensation and even icing is essential.

6.4 A Look Into Future Work

This section will showcase the future possibilities of this thesis, highlighting potential areas for improvement and recommended fixes to ensure more consistent results. The future work section will be divided into two parts: improvements to be made in the heat exchanger test rig and the importance of continued efforts on the numerical methods and solvers.

6.4.1 Heat exchanger and test rig

Addressing the rig's issues is a priority, as evident from both this thesis and the bachelor's thesis [28]. While the plexiglass enclosure is a good concept, it fogs up quickly, obscuring visibility inside. Two potential solutions are proposed: either transforming the air side of the rig into a wind tunnel, requiring adjustments to control flow conditions, or implementing heating elements within the plexiglass enclosure to prevent condensation on the glass. Similarly, these heating elements could enhance observation by preventing fogging on the glass of the heat exchanger test section.

The second item is to refine the implementation of the measuring devices. The measurements from the tests must be useful and trustworthy. Hence better implementation of pressure probes should be done. The pressure drop reading should be coherent with the Kays and London data before implementing other complexities. The temperature probes should be tested and both the air and coolant temperatures must produce accurate results. The air side has higher temperatures and temperature changes and could therefore remain the same, whereas the coolant changes with less than one degree and it would be important to capture this accurately for heat transfer calculation comparisons. Implementing better cameras and camera angles would be beneficial for a clearer picture. Infrared (IR) cameras could be useful for the validation of ice thickness once the numerical models produce promising results. This allows direct comparisons of ice thickness on the tubes. A final requirement would be to automate the data collection process. This would save the data directly in a file with timestamps making data collection simpler and the post-processing job shortened, less tedious, and less prone to human error.

The heat exchanger in these tests only implemented three functioning rows. For a more complete observation of this system, all tubes need to be connected to the cooling system. It is therefore very important to figure out where unnecessary temperature losses occur and how to mitigate these to keep the test running for the longest possible time. As could be seen from the result the test needs around two minutes to display the first ice and over 10 minutes for bulk ice. Manifolds were produced to collect all the tubes, these could produce unwanted pressure losses and should be designed to ensure minimal losses.

Once all of the above-mentioned topics are covered and produce good results, the heat exchanger could be tested under various speeds, temperatures in air and water, and finally humidity levels. A performance map can be created for this exchanger. Other heat exchangers could eventually also be tested by replacing the test section.

6.4.2 Continued effort on numerical methods

As the ϵ-NTU is an effective method for single-phase heat exchangers it fell short in this case where it did not take into account the multiphase behaviors. Incorporating compensation for humid air, condensation, and hopefully ice accretion would make the sizing code more accurate. Therefore, there is a large importance in investigating how to address this in a code.

The CFD methodology utilized the standard settings and yielded no meaningful correspondence to real-life experiments. This indicates the need for a deeper understanding of multiphase modeling in heat exchanger CFD. Adjusting the parameters is a must for achieving improved results and therefore a much-needed continuation of the project.

6.5 Summary and Fulfillment of Purpose

The primary goal of the project was to dimension, build, and test a heat exchanger in a test facility constructed for the specific reason of freezing. This was achieved as can be seen in section 4.1 and 4.4. In addition to this, the project set out to investigate numerical methods through CFD solution where the results can be seen in sections 4.2 and 4.4. With this, the thesis fulfilled its purpose.

Bibliography

[1] European Comission. "The european green deal." (2019), [Online]. Available: `https://commission.europa.eu/strategy-and-policy/priorities-2019-2024/european-green-deal_en` (visited on 01/29/2024).

[2] D. Verstraete, "The potential of liquid hydrogen for long range aircraft propulsion," 2009.

[3] F. M. Troeltsch, M. Engelmann, A. E. Scholz, F. Peter, J. Kaiser, and M. Hornung, "Hydrogen powered long haul aircraft with minimized climate impact," in *AIAA Aviation 2020 forum*, 2020, p. 2660.

[4] M. H. McCay and S. Shafiee, "22 - hydrogen: An energy carrier," in *Future Energy (Third Edition)*, T. M. Letcher, Ed., Third Edition, Elsevier, 2020, pp. 475–493, ISBN: 978-0-08-102886-5. DOI: `https://doi.org/10.1016/B978-0-08-102886-5.00022-0`. [Online]. Available: `https://www.sciencedirect.com/science/article/pii/B9780081028865000220`.

[5] T. Burschyk, Y. Cabac, D. Silberhorn, B. Boden, and B. Nagel, "Liquid hydrogen storage design trades for a short-range aircraft concept," *CEAS Aeronautical Journal*, vol. 14, no. 4, pp. 879–893, 2023.

[6] R. Shah and D. Sekulic, "Heat exchangers," *Handbook of heat transfer*, vol. 3, 1998.

[7] P. Łapka, M. Seredyński, and A. Ćwik, "Preliminary study on supercritical hydrogen and bleed air heat exchanger for aircraft application," *Proceedings of the Institution of Mechanical Engineers, Part G: Journal of Aerospace Engineering*, vol. 232, no. 12, pp. 2231–2243, 2018.

[8] H. Abedi, C. Xisto, I. Jonsson, T. Grönstedt, and A. Rolt, "Preliminary analysis of compression system integrated heat management concepts using lh2-based parametric gas turbine model," *Aerospace*, vol. 9, no. 4, p. 216, 2022.

[9] T. Richter, "Concerning the freezing of condensate in the plate heat exchanger," *Hoval Aktiengesellschaftr*, vol. 1, 2018.

[10] S. Anisimov, A. Jedlikowski, and D. Pandelidis, "Frost formation in the cross-flow plate heat exchanger for energy recovery," *International Journal of Heat and Mass Transfer*, vol. 90, pp. 201–217, 2015.

[11] R. D. Blevins, "Flow-induced vibration," *New York*, 1977.

[12] E. Schlünder, I. C. for Heat, and M. Transfer, *Heat Exchanger Design Handbook* (Heat Exchanger Design Handbook v. 1-5). Hemisphere Publishing Corporation, 1983, ISBN: 9780891161257. [Online]. Available: `https://books.google.se/books?id=NMQRAQAAMAAJ`.

[13] W. M. Kays and A. L. London, *Compact Heat Exchanger*. United States of America: McGraw-Hill Book Company, 1955, 1964.

[14] F. P. Incropera, D. P. Dewitt, T. L. Bergman, and A. S. Lavine, *Fundemantals of Heat and Mass Transfer*. United States of America: John Wiley & Sons, 2007.

[15] D. G. Wilson and T. Korakianitis, *The Design of High-Efficiency Turbomachinery and Gas Turbines*. United States of America: The MIT Press, 2014.

[16] B. Petukhov, "Heat transfer and friction in turbulent pipe flow with variable physical properties," in ser. Advances in Heat Transfer, J. P. Hartnett and T. F. Irvine, Eds., vol. 6, Elsevier, 1970, pp. 503–564. DOI: `https://doi.org/10.1016/S0065-2717(08)70153-9`. [Online]. Available: `https://www.sciencedirect.com/science/article/pii/S0065271708701539`.

[17] V. Gnielinski, "New equations for heat and mass transfer in turbulent pipe and channel flow," 1976. [Online]. Available: `https://api.semanticscholar.org/CorpusID:136639967`.

[18] H. Zheng, "Chapter 3 - fundamental relationships of heat and mass transfer in solar seawater desalination systems," in *Solar Energy Desalination Technology*, H. Zheng, Ed., Amsterdam: Elsevier, 2017, pp. 173–258, ISBN: 978-0-12-805411-6. DOI: `https://doi.org/10.1016/B978-0-12-805411-6.00003-8`. [Online]. Available: `https://www.sciencedirect.com/science/article/pii/B9780128054116000038`.

[19] J. Shin and T. H. Bond, "Experimental and computational ice shapes and resulting drag increase for a naca 0012 airfoil," in *California State Univ., The Fifth Symposium on Numerical and Physical Aspects of Aerodynamic Flows*, 1992.

[20] S. G. Pouryoussefi, M. Mirzaei, M.-M. Nazemi, M. Fouladi, and A. Doostmahmoudi, "Experimental study of ice accretion effects on aerodynamic performance of an naca 23012 airfoil," *Chinese Journal of Aeronautics*, vol. 29, no. 3, pp. 585–595, 2016, ISSN: 1000-9361. DOI: `https://doi.org/10.1016/j.cja.2016.03.002`. [Online]. Available: `https://www.sciencedirect.com/science/article/pii/S100093611630019X`.

[21] Y. Liu, K. Zhang, W. Tian, and H. Hu, "An experimental investigation on the dynamic ice accretion and unsteady heat transfer over an airfoil surface with embedded initial ice roughness," *International Journal of Heat and Mass Transfer*, vol. 146, p. 118 900, 2020, ISSN: 0017-9310. DOI: `https://doi.org/10.1016/j.ijheatmasstransfer.2019.118900`. [Online]. Available: `https://www.sciencedirect.com/science/article/pii/S0017931019342814`.

[22] S. Wilensky. "Ice accretion and ice protection in star-ccm+." (), [Online]. Available: `https://support.sw.siemens.com/en-US/knowledge-base/KB000054198_EN_US`.

[23] S. Anisimov, A. Jedlikowski, and D. Pandelidis, "Frost formation in the cross-flow plate heat exchanger for energy recovery," *International Journal of Heat and Mass Transfer*, vol. 90, pp. 201–217, 2015, ISSN: 0017-9310. DOI: `https://doi.org/10.1016/j.ijheatmasstransfer.2015.06.056`. [Online]. Available: `https://www.sciencedirect.com/science/article/pii/S001793101500678X`.

[24] Siemens. "Dispersed multiphase (dmp) theory." (), [Online]. Available: `file:///C:/Program%20Files/Siemens/18.02.010/STAR-CCM+18.02.010/doc/en/online/STARCCMP/GUID-047974D5-D783-4567-BEA2-A6AC2ED3A480.html`.

[25] Siemens. "Fluid film theory." (), [Online]. Available: `file:///C:/Program%20Files/Siemens/18.02.010/STAR-CCM+18.02.010/doc/en/online/STARCCMP/GUID-853860C9-6C1F-4AEF-979F-732B55913167.html#GUID-853860C9-6C1F-4AEF-979F-732B55913167__ID-1723-00000909`.

[26] Siemens. "Dispersed multiphase (dmp)." (), [Online]. Available: `file:///chalmers/sw/sup64/star-ccm+2310-r8/18.06.006-R8/STAR-CCM+18.06.006-R8/doc/en/online/STARCCMP/GUID-033EF985-3841-4392-9DC0-7893BB17EC66.html`.

[27] Siemens. "Dispersed multiphase (dmp)." (), [Online]. Available: `file:///chalmers/sw/sup64/star-ccm+2310-r8/18.06.006-R8/STAR-CCM+18.06.006-R8/doc/en/online/STARCCMP/GUID-F74F7E33-2DAC-4958-90A2-E01F9E68F34D.html`.

[28] P. Miltén, "Experimentell undersökning ac kondensering på rör i värmeväxlare [experimental investigation of condensate and freezing on tubes in a heat exchanger]," *Thesis in maritime engineering program*, 2024.

[29] T. C. Company. "Hm1500lf relative humidity module." (), [Online]. Available: `https://www.te.com/commerce/DocumentDelivery/DDEController?Action=showdoc&DocId=Data+Sheet%7FHPC062_F%7FA%7Fpdf%7FEnglish%7FENG_DS_HPC062_F_A.pdf%7FCAT-HSA0002`.

A

Hand calculation sizing

Assume:

1. Air inlet temperature
2. Coolant inlet temperature
3. Dimension tubing

This will result in a guess of a Reynolds number. An initial guess is 7000 but later it can be shown that anything above 1000 should be enough.

Therefore assume the following is known:

1. T_{air} =50C
2. T_{cool} =-20C

Use the following equations to find a reasonable coolant volume needed, a reasonable number of tubes, and an acceptable temperature drop.

$$Re = \frac{vd}{k} \tag{A.1}$$

$$A = m * n * L \tag{A.2}$$

Assume reasonable U as

1. U = 200 $W/m^2/k$

Therefore Q= 2800 W Assume some volume needed for the coolant and the it is possible to estimate a Kelvin drop per second. If 40 liters is assumed which is approximately 40 kg. The specific heat could be assumed as 3500 J/kgK

$$seconds/kelvin = 40 \cdot 3500/2800 = 50s/k \tag{A.3}$$

This process was repeated before achieving the above mentioned values. But the shown values are where the initial assumption ended up. Which resulted in a 8x8 configuration with a decent temperature drop.

B

Kays and London S150-125 HEX

Tabulated data from Kays and Londons compact heat exchanger regarding the S150-125 heat exchanger.

TABLE X
Dimensions of the S150-125 HEX

Diameter (in.)	**Transvers spacing (in.)**	**Longitudinal spacing (in.)**	$\boldsymbol{D_h (in.)}$	$\boldsymbol{\sigma}$	$\boldsymbol{\alpha [ft^2/ft^3]}$
0.375	0.5635	0.4688	0.0298	0.333	53.4

TABLE XI
Tabulated values from kays and london

$\boldsymbol{R_e}$	$\boldsymbol{S_t P_r^{2/3}}$	$\boldsymbol{f}$
15000	0.00690	0.0503
12000	0.00753	0.0525
10000	0.00808	0.0543
8000	0.00883	0.0566
6000	0.00987	0.0596
5000	0.0106	0.0615
4000	0.0116	0.0641
3000	0.0129	0.0675
2500	0.0138	0.0700
2000	0.0151	0.0728
1500	0.0169	0.0768
1200	0.0184	0.0800
1000	0.0198	0.0828
800	0.0216	0.0850
600	0.0241	0.0907
500	0.0258	0.0940

Dimensions of the HEX can be seen in the images below:

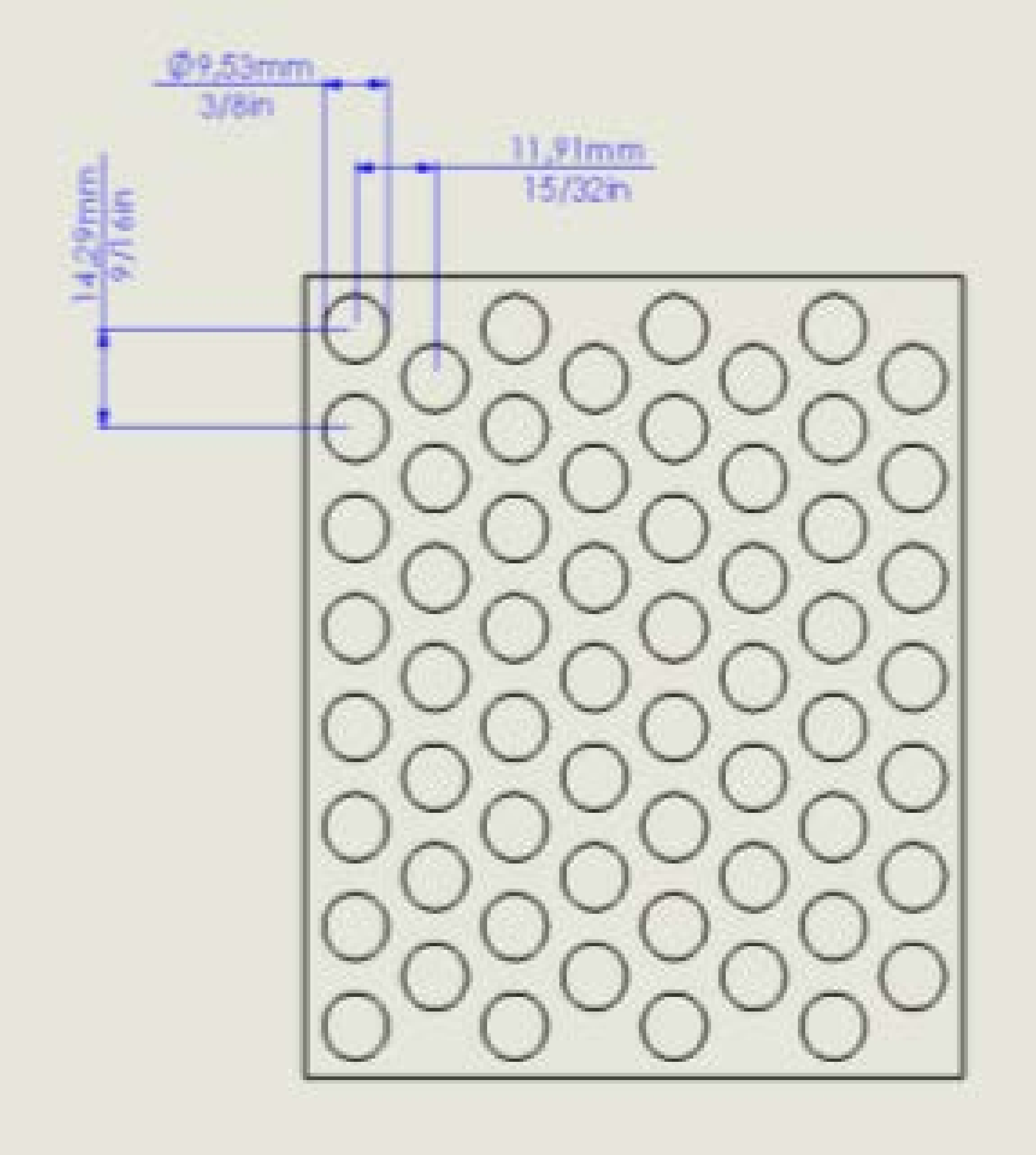

Fig. 32. Dimensions regarding spacing of tubes in the HEX in question.

C

Sizing code

```
## Sizing V2
import numpy as np
import matplotlib.pyplot as plt
from pyfluids import Fluid, FluidsList, Input
import pandas as pd
import plotly.graph_objects as plt
from plotly.subplots import make_subplots
from pyfluids import Fluid, FluidsList, Input

## Here we go off using the s150125 HEX
# Import DATA from K&L
file_path = "C:\\Users\\olive\\Desktop\\Not a master thesis\\Code\\f_150125.txt"
data_f150125 = pd.read_csv(file_path, sep=';')
Re_150125 = np.flip(data_f150125['Re'].values)
StPr23_150125 = np.flip(data_f150125['StPr'].values)
f150125 = np.flip(data_f150125['f'].values)

# Tubing inputs:
m = 8 # rows wanted
n = 8 # columns wanted
D_tube_o = 2.54*(3/8)*0.01 #0.01 # Diameter of individual tube in [m]
D_tube_i = D_tube_o-0.0005
L_tube = D_tube_o*10 # If we want a 1:10 relation
s_x = (15/32)*25.4/1000 # inch to mm to m
s_y = (9/16)*25.4/1000
D_h_s150125 = 0.0249*0.3048 # ft to m
D_h_air_in = D_h_s150125
V_HEX = (n*s_y)*(s_x*m)*L_tube
Axy = (n*s_y)*(s_x*m)
Axz = (s_x*m)*L_tube
Ayz = (s_y*n)*L_tube

D_tube_o_scaled = 0.01
D_tube_i_scaled = D_tube_o_scaled - 0.0005
scalingFactor1 = D_tube_o_scaled/D_tube_o
scalingFactor2 = D_tube_i_scaled/D_tube_i
L_tube_scaled = D_tube_o_scaled * 10
s_x_scaled = scalingFactor1 * s_x
s_y_scaled = s_y * scalingFactor1
D_h_air_in_scaled = D_h_s150125 * scalingFactor1
V_HEX_scaled = (n*s_y_scaled)*(s_x_scaled*m)*L_tube_scaled
Axy_scaled = (n*s_y_scaled)*(s_x_scaled*m)
```

```
Axz_scaled = (s_x_scaled*m)*L_tube_scaled
Ayz_Scaled = (s_y_scaled*n)*L_tube_scaled

print('A non scaled HEX 150125 has the following dimensions')
print(f'Outer diameter of pipe: {D_tube_o} [m]')
print(f'Inner diameter of pipe: {D_tube_i} [m]')
print(f'The corresponding [x,y,z] lentghs: [{m*s_x},{n*s_y},{L_tube
    }]')
print(f'Total space volume of the HEX: {V_HEX} m\u00B3')
print(f'Area in xy plane: {Axy} [m\u00B2]')
print(f'Area in xz plane: {Axz} [m\u00B2]')
print(f'Area in yz plane: {Ayz} [m\u00B2]')
print('A scaled HEX according to 150125 will have:')
print(f'Outer diameter of pipe: {D_tube_o_scaled} [m]')
print(f'Inner diameter of pipe: {D_tube_i_scaled} [m]')
print(f'The corresponding [x,y,z] lentghs: [{m*s_x_scaled},{n*
    s_y_scaled},{L_tube_scaled}]')
print(f'Total space volume of the HEX: {V_HEX_scaled} m\u00B3')
print(f'Area in xy plane: {Axy_scaled} [m\u00B2]')
print(f'Area in xz plane: {Axz_scaled} [m\u00B2]')
print(f'Area in yz plane: {Ayz_Scaled} [m\u00B2]')

## Input massflows
m_dot_air = np.linspace(0.0045,0.142,500)
m_dot_cool = np.linspace(0.1,0.5,499) # kg/s
m_dot_air = np.repeat(m_dot_air[:, np.newaxis], np.shape(m_dot_cool
    )[0], axis=1)
m_dot_cool = np.repeat(m_dot_cool[np.newaxis,:], np.shape(m_dot_air
    )[0], axis=0)
# Input air side 0.05 to 1.4
T_in_air = 50+273.15
P_air_amb = 1.01325*10**5 # Assume atmospheric
rho_air_in = P_air_amb/(287.0500676*T_in_air) # ideal gas law to
    find out air temp
mu_air_in = 19.63*10**(-6) # Dynamic viscosity at 50 deg C in [kg/(
    ms)]
nu_air_in = mu_air_in/rho_air_in
h_tc_air = 200
c_p_air = 1.007 * 1000
# K konstnat
k_wall = 120 #thermal conductivity fo stee material
k_air = 0.607 # Thermal conductivity for air
k_cool =  0.598 # thermal conductivity of coolant

# Input coolant side
T_cool_in = -20 + 273.15 # Temperature of coolant in cold cicruit (
    deg celcius
P_cool_in = 1.01325*10**5 # Assume atmospheric
monoethylene_glycol = Fluid(FluidsList.MEG, 50).with_state(
    Input.pressure(P_cool_in), Input.temperature(-20)
)

nu_cool_in = monoethylene_glycol.kinematic_viscosity
#25*10**-6#
rho_cool_in = monoethylene_glycol.density
#110#
```

```python
mu_cool_in = monoethylene_glycol.dynamic_viscosity
#25.50*10**-3#
c_p_cool = monoethylene_glycol.specific_heat
#3.11*1000#
print(nu_cool_in,rho_cool_in,mu_cool_in,c_p_cool)

#for i in range(np.size(m_dot_air)):
### Find outputs coolant side
A_tube = (1/4)*np.pi*(D_tube_i)**2
v_cool = m_dot_cool/(rho_cool_in*A_tube*m*n)
Re_cool = (v_cool*D_tube_i)/nu_cool_in

### Find output air side dP
# calc Re with m_dot
# start with pressure drop, equation given by kays and lond
A_air_EFF = (L_tube*(n*s_y))-(D_tube_o*L_tube*n)
alpha_air = 53.4 *((0.3048**2)/(0.3048**3))# Given for 150125 given in ft**2/ft**3
# Aa = (L_tube*(n*s_y))*0.333

G_air = m_dot_air/A_air_EFF
Re_air = (D_h_air_in*G_air)/mu_air_in
m_dot_150125 = Re_150125 * mu_air_in * A_air_EFF/ D_h_air_in
G_air_150125 = m_dot_150125/A_air_EFF
f_air_int = np.interp(Re_air,Re_150125,f150125)
voidf_air = 0.333
#A_air_HTA = voidf_air * A_air_EFF
# If we assume the densities are the same at 1 and 2  then we get the pressure drop as a function of friction f
P_air_Delta = (m_dot_air**2/(2*(L_tube*(n*s_y))**2))*(f_air_int*(alpha_air/voidf_air**3)*m*s_x*(1/rho_air_in))
#(G_air**2 / 2) * (f_air_int* (alpha_air/voidf_air**3) * L_tube * (1/rho_air_in))
#(G_air**2)/(2)*1/rho_air_in*(f_air_int*(alpha_air*n*s_y*m*s_x*L_tube/A_air_EFF))

P_air_Delta_150125 =(m_dot_150125**2/(2*(L_tube*(n*s_y))**2))*(f150125*(alpha_air/voidf_air**3)*m*s_x*(1/rho_air_in))
#(G_air**2/2) * (f150125*(alpha_air/voidf_air**3) * L_tube * (1/rho_air_in))
#((G_air_150125**2)/(2))*(1/rho_air_in)*(f150125*(alpha_air*n*s_y*m*s_x*L_tube/A_air_EFF))
# Generate points for the fitted line
params = np.polyfit(np.log(m_dot_150125), np.log(f150125), 1)
m_dot_150125_fit, f150125_fit = params
m_dot_150125_fit_fit = np.linspace(min(m_dot_150125), max(m_dot_150125), 100)
f150125_fit_fit = np.exp(f150125_fit) * m_dot_150125_fit_fit**m_dot_150125_fit

## All the dimensionless values for air
Pr_150125_air = mu_air_in*c_p_air / k_air # konstant always basically
St_150125 = StPr23_150125/(Pr_150125_air**(2/3))
StPr23_air_int = np.interp(Re_air,Re_150125,StPr23_150125) # interpolated j values
```

```
St_air_int = StPr23_air_int/(Pr_150125_air**(2/3)) # interpolated St values
Nu_150125 = St_150125*Re_150125*Pr_150125_air
Nu_air_int = St_air_int*Re_air*Pr_150125_air # Interpolate Nu values
h_150125 = (Nu_150125*k_air)/D_h_s150125
h_air_int = (Nu_air_int*k_air)/D_h_air_in # Interpolated h values for air

## All dimensionless numbers for coolant
# Flag which records if the Reynolds number is outside its bounds
Pr_cool = mu_cool_in*c_p_cool/k_cool
#Sigmoid properties
ReMidPoint = 2700
#Heat transfer correlation for circular pipes
sigmoid = 1 / (1 + np.exp(-k_cool * (Re_cool - ReMidPoint)))
fLam = 64 / Re_cool
NuLam = 3.66
fTurb = (0.79 * np.log(Re_cool) - 1.64) ** -2  # petukhov
NuTurb = ((fTurb / 8) * (Re_cool - 1000) * Pr_cool) / (1 + 12.7 * ((fTurb / 8) ** 0.5) * (Pr_cool ** (2 / 3) - 1))  # gnielinski
f_cool = (1 - sigmoid) * fLam + sigmoid * fTurb
Nu_cool = (1 - sigmoid) * NuLam + sigmoid * NuTurb
h_cool = (Nu_cool * k_cool) / L_tube
### Find output coolant side dP
#G_cool = m_dot_cool/(A_tube*m*n)
#alpha_air_2 =( n*m*D_tube_o*L_tube*np.pi )/ (n*s_y*L_tube*m*s_x)

alpha_cool = (m*n*np.pi*(D_tube_i)) / (m*n*s_x*s_y*L_tube) # ? this one is too small
#(L_tube*np.pi*(D_tube_i)*m*n) / (m*n*s_x*s_y*L_tube) # ?
voidf_cool = (m*n*np.pi*(1/4)*D_tube_i**2)/(np.abs((n*s_y*m*s_x)-(m*n*np.pi*(1/4)*D_tube_i**2)))
print((m*n*np.pi*(1/4)*D_tube_i**2))
P_cool_Delta = (m_dot_cool**2/(2*(A_tube*m*n)**2))*(f_cool*(alpha_cool/voidf_cool**3)*L_tube*(1/rho_cool_in))

#### dT is dependant on each other hence need to be done at the end
print(m_dot_air)
print(m_dot_cool)
print('____________')
C_air = c_p_air*m_dot_air
C_cool = c_p_cool*m_dot_cool
print(C_air)
print(C_cool)
print('____________')
C_min = np.minimum(C_air, C_cool)
C_max = np.maximum(C_air, C_cool)
print(C_min)
print(C_max)
print('____________')
Cr = C_min/C_max
print('____________')
print(Cr)
#
A_h = alpha_air * m*n*s_x*s_y*L_tube
```

```
A_c = alpha_cool * m*n*s_x*s_y*L_tube
A_w = (A_h + A_c) / 2
U_air = 1/((1/(h_air_int))+((D_tube_o-D_tube_i)/((A_w/A_h)*k_wall))+(1/((A_c/A_h)*h_cool)))
print(U_air)
print('____________')
#U_cool = 1/((1/(h_cool))+((D_tube_o-D_tube_i)/((A_w/A_c)*k_wall))+(1/((A_h/A_c)*h_air_int)))

NTUmax_air = n*s_y*m*s_x*L_tube*alpha_air*U_air/C_min
eps = 1-np.exp(-NTUmax_air)
print(eps)
print('____________')
#1-np.exp(-NTUmax_air)
#1-np.exp(-Cr**(-1)*(1-np.exp(-Cr*NTUmax_air)))
#1-np.exp((1/Cr)*NTUmax_air**.22*(np.exp(-Cr*NTUmax_air**.78)-1))
dT0_air = -eps*(C_min/C_air)*(T_in_air-T_cool_in)  #(f1.T0[-2]-f2.T0[-2])
dT0_cool = eps*(C_min/C_cool)*(T_in_air-T_cool_in)
print(dT0_air)
print(dT0_cool)
print('____________')
print(m_dot_air[:,0])
print(m_dot_cool[0,:])
# ------------------------------------------------------------------------------ #
```

Listing C.1: Python sizing code

subcaption

D

CFD setup

This appended section will describe the setup of the simulation in Starccm+.

D.1 Why Starccm+

Starccm+ provides a good baseline simulation providing both a mesher and solver in one software. The disadvantage of StarCCM+ is that it is not open source and hence the resources are only accessible to customers. As Chalmers possesses a license to operate Starccm and it being part of the education, the time saved would prove beneficial. Siemens SimCenter provides documentation on many subjects, one of which being multiphase solutions regarding icing. Such documentation also provides validations cases and therefore solidifies the argument for using the selected solvers and settings.

D.2 Domain

The domain used could be thought of in two ways, the first being the entire construction, the other being partial construction with symmetry boundaries. Both of these should be representative of the conditions observed in the test section of a heat exchange. The two types of domains can be seen in the figure below:

The usage of the symmetrical domain is for fast prototyping and fast results whereas the full domain should always be used in case of comparison to real-life tests.

D.3 Mesh

The mesh for the main domain (with all the tubes) was constructed with the practices that Starccm recommends. A mesh study was also conducted to support the final mesh. The mesh study that was constructed looked like this: It can then be seen that, for a rapidly increasing number of cells, the accuracy of the solution does not vary significantly. Hence, choosing a base size of 10mm would seem reasonable and is what is used in the thesis. The meshers is an automated mesher with a trimmed cell prism layer type. The mesh is set up with a bulk mesh and a refinement region containing the tubes to resolve the behavior better in between the tubes.

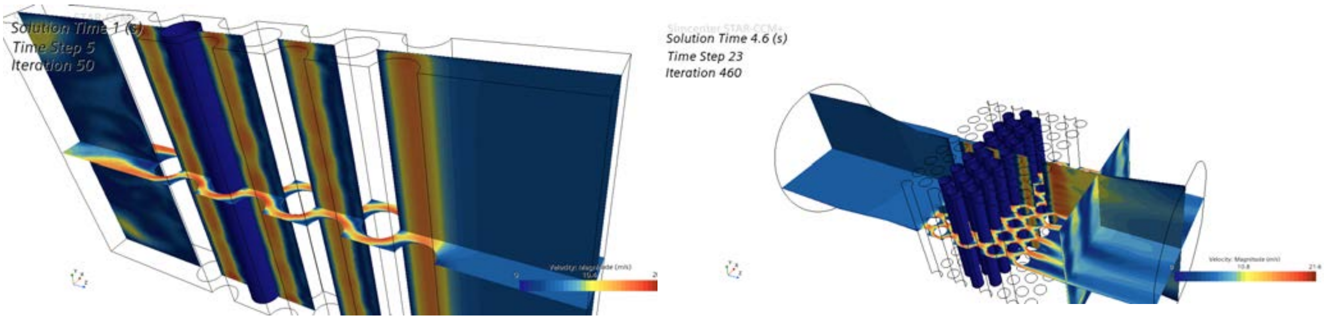

((a)) Symmetrical domain.

((b)) Entire rig domain.

Fig. 33. Different types of usable domains.

TABLE XII
Mesh study test plan

Base size (mm)	Refinemtent %	Prism layers	Velocity magnitude at plane	Cptot at plane	Nr. of cells
10	7	12	6.319764	-1028.994	11109315
9	7	12	7.70682	-1029.732	14327488
8	7	12	7.825943	-1035.558	18590934
7	7	12	7.759855	-1034.985	24559810
6	7	12	7.968749	-1022.014	35219123

D.4 Solver Setting

DMP continua:

- Eulerian Phase with constant density and assuming liquid.

Fluid Film continua:

- Film phase with constant density and assuming laminar liquid regime
- Melting-solidification with an under-relaxation factor of 1
- Segregated fluid film temperature of the first order
- Solidified film removal with 6 smoothing steps and a solid time factor of 20

A multiphase interaction continuum was used to link the Film-DMP, DMP-air, and film-air interactions.

Remeshing was used for the automated mesh:

- Min. cel volume of zero

- Checking both cell volume and face validity with a minimum face validity of 0.5

Phase condition of the DMP phase was set to 6.816E-7 on the inlet region.
Implicit unsteady silver had a time step of 0.2s using first-order temporal discretization. The remesher had high verbosity and was triggered by a relevant delta time of 10s. In this case, 10 inner iterations were used.

E

Tables from Icing Test

Here the gathered raw data from the two icing tests are presented in table format.

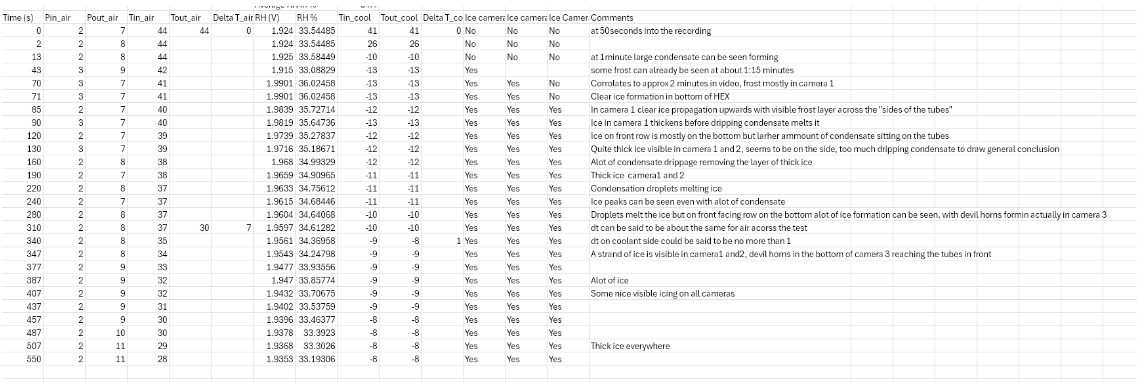

Time (s)	Pin_air	Pout_air	Tin_air	Tout_air	Delta T_air	RH (V)	RH %	Tin_cool	Tout_cool	Delta T_co	Ice camera	Ice camera	Ice Camer	Comments
0	2	7	44	44	0	1.924	33.54485	41	41	0	No	No	No	at 50seconds into the recording
2	2	8	44			1.924	33.54485	26	26		No	No	No	
13	2	8	44			1.925	33.58449	-10	-10		No	No	No	at 1minute large condensate can be seen forming
43	3	9	42			1.915	33.08829	-13	-13		Yes			some frost can already be seen at about 1:15 minutes
70	3	7	41			1.9901	36.02458	-13	-13		Yes	Yes	No	Corrolates to approx 2 minutes in video, frost mostly in camera 1
71	3	7	41			1.9901	36.02458	-13	-13		Yes	Yes	No	Clear ice formation in bottom of HEX
85	2	7	40			1.9839	35.72714	-12	-12		Yes	Yes	Yes	In camera 1 clear ice propagation upwards with visible frost layer across the "sides of the tubes"
90	3	7	40			1.9819	35.64736	-13	-13		Yes	Yes	Yes	Ice in camera 1 thickens before dripping condensate melts it
120	2	7	39			1.9739	35.27837	-12	-12		Yes	Yes	Yes	Ice on front row is mostly on the bottom but larher ammount of condensate sitting on the tubes
130	3	7	39			1.9716	35.18671	-12	-12		Yes	Yes	Yes	Quite thick ice visible in camera 1 and 2, seems to be on the side, too much dripping condensate to draw general conclusion
160	2	8	38			1.968	34.99329	-12	-12		Yes	Yes	Yes	Alot of condensate drippage removing the layer of thick ice
190	2	7	38			1.9659	34.90965	-11	-11		Yes	Yes	Yes	Thick ice camera1 and 2
220	2	8	37			1.9633	34.75612	-11	-11		Yes	Yes	Yes	Condensation droplets melting ice
240	2	7	37			1.9615	34.68446	-11	-11		Yes	Yes	Yes	Ice peaks can be seen even with alot of condensate
280	2	8	37			1.9604	34.64068	-10	-10		Yes	Yes	Yes	Droplets melt the ice but on front facing row on the bottom alot of ice formation can be seen, with devil horns formin actually in camera 3
310	2	8	37	30	7	1.9597	34.61282	-10	-10		Yes	Yes	Yes	dt can be said to be about the same for air acorss the test
340	2	8	35			1.9561	34.36958	-9	-8	1	Yes	Yes	Yes	dt on coolant side could be said to be no more than 1
347	2	8	34			1.9543	34.24798	-9	-9		Yes	Yes	Yes	A strand of ice is visible in camera1 and2, devil horns in the bottom of camera 3 reaching the tubes in front
377	2	9	33			1.9477	33.93556	-9	-9		Yes	Yes	Yes	
387	2	9	32			1.947	33.85774	-9	-9		Yes	Yes	Yes	Alot of ice
407	2	9	32			1.9432	33.70675	-9	-9		Yes	Yes	Yes	Some nice visible icing on all cameras
437	2	9	31			1.9402	33.53759	-9	-9		Yes	Yes	Yes	
457	2	9	30			1.9396	33.46377	-8	-8		Yes	Yes	Yes	
487	2	10	30			1.9378	33.3923	-8	-8		Yes	Yes	Yes	
507	2	11	29			1.9368	33.3026	-8	-8		Yes	Yes	Yes	Thick ice everywhere
550	2	11	28			1.9353	33.19306	-8	-8		Yes	Yes	Yes	

Fig. 34. Image of the entire rawdata table.

Time (s)	Pin_air	Pout_air	Tin_air	Tout_air	Delta T_air	RH (v)	RH%	Tin_cool	Tout_cool	Delta T_co	Ice camera	Ice camera	Ice Camer	Picture	Comments
0	6	25	44	44	0	2.622	61.70298	41	41	0	No	No	No		at 50seconds into the recording
2	6	25	44			2.622	61.70298	26	26		No	No	No		
20	7	25	41.9			2.622	61.59798	-13	-12		No	No	No		
30	7	26	41.8			2.621	61.55286	-11			No	No	No		
50	7	22	40.2			2.623	61.5531	-11	-11		No	No	No		The fans malfunctioned slightly after this point, no need to doccument time to ice since no ice ever formed
120	6	52	37			2.624	61.43321	-9	-8		No	No	No		
130	5	54	36.6			2.623	61.3731	-9			No	No	No		
155	6	61	35.3			2.624	61.34821	-9			No	No	No		
175	5	65	35.8	30	5.8	2.624	61.37321	-9	-8		No	No	No		
195	5	71	35.6			2.624	61.36321	-8			No	No	No		
205	5	70	35.8			2.623	61.3331	-9			No	No	No		
225	6	79	35.6			2.625	61.40332	-9			No	No	No		
245	6	83	35.3			2.625	61.38832	-9			No	No	No		At 6Pa no ice was formed

Fig. 35. Image of the entire rawdata table.

F

Detailed Documentation of results

Here a a link to images and recordings of the tests:

Here are the images referred to in the document.

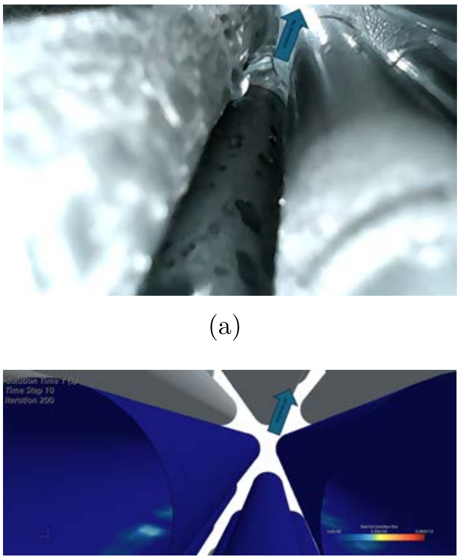

(a)

(b)

Fig. 36. (a) Experiment, (b) CFD, at the start of the experiment (approximately 20s) from camera 1 (see 11).

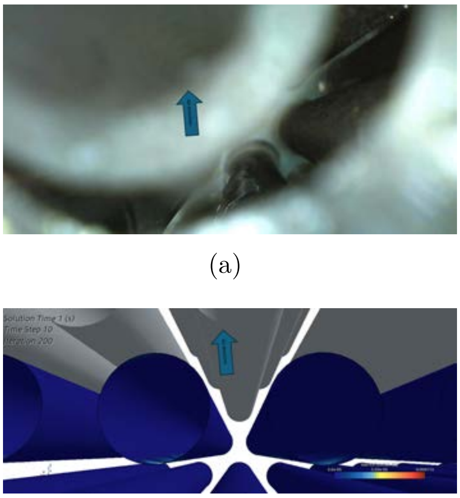

(a)

(b)

Fig. 37. (a) Experiment, (b) CFD, at the start of the experiment (approximately 20s) from camera 2 (see 11).

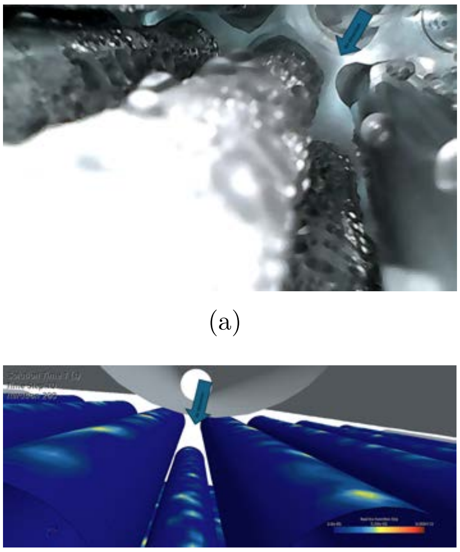

(a)

(b)

Fig. 38. (a) Experiment, (b) CFD, at the start of the experiment (approximately 20s) from camera 3 (see 11).

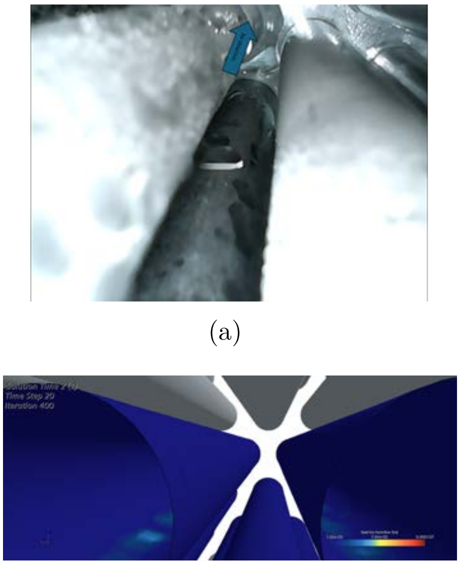

(a)

(b)

Fig. 39. (a) Experiment, (b) CFD, at 40 seconds into the experiment from camera 1 (see 11).

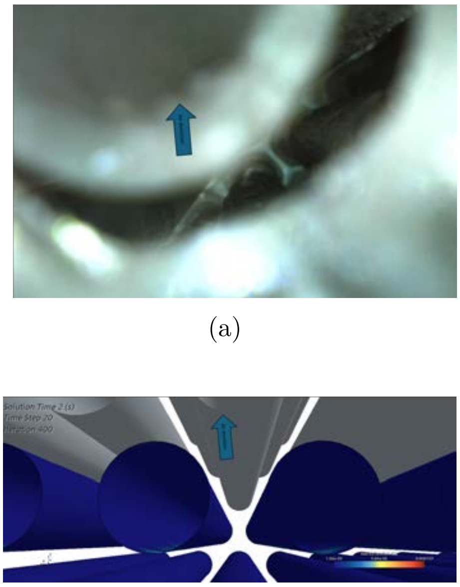

(a)

(b)

Fig. 40. (a) Experiment, (b) CFD, at 40 seconds into the experiment from camera 2 (see 11).

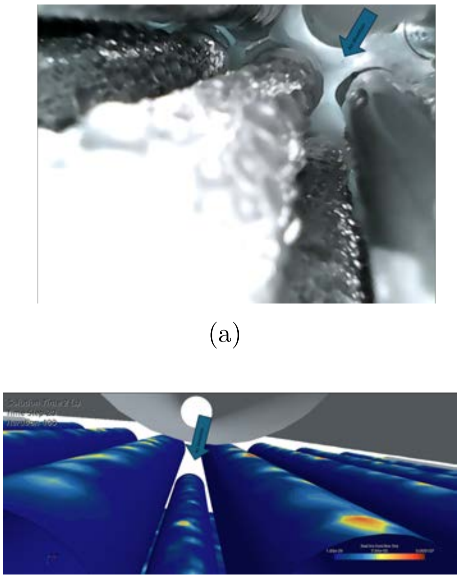

(a)

(b)

Fig. 41. (a) Experiment, (b) CFD, at 40 seconds into the experiment from camera 3 (see 11).

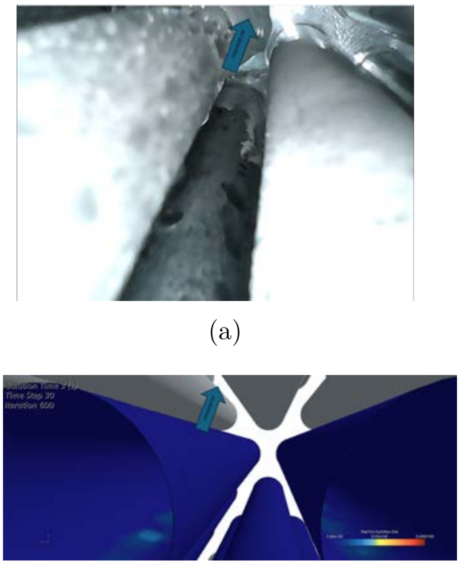

(a)

(b)

Fig. 42. (a) Experiment, (b) CFD, at ≈71 seconds into the experiment from camera 1 (see 11).

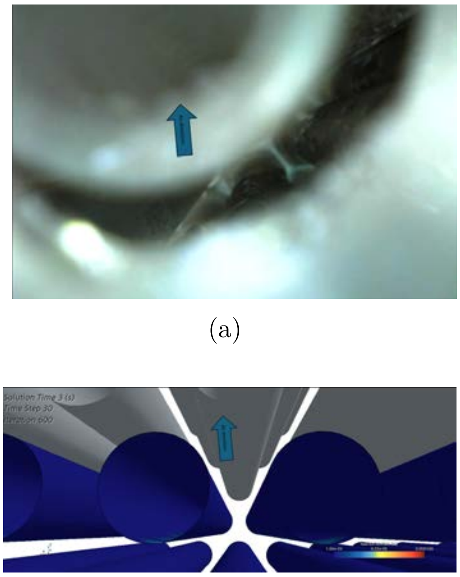

(a)

(b)

Fig. 43. (a) Experiment, (b) CFD, at ≈71 seconds into the experiment from camera 2 (see 11).

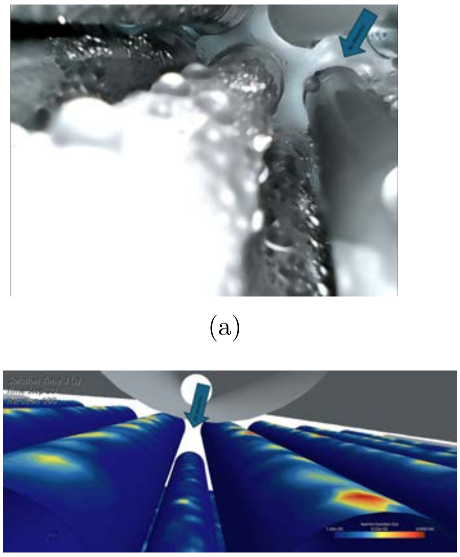

(a)

(b)

Fig. 44. (a) Experiment, (b) CFD, at ≈71 seconds into the experiment from camera 3 (see 11).

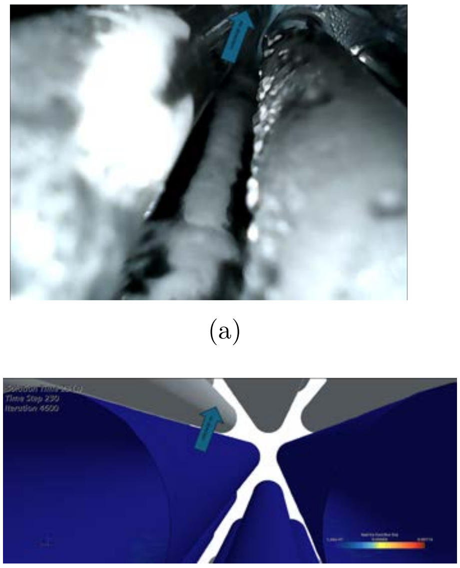

(a)

(b)

Fig. 45. (a) Experiment, (b) CFD, at ≈470 seconds into the experiment from camera 1 (see 11).

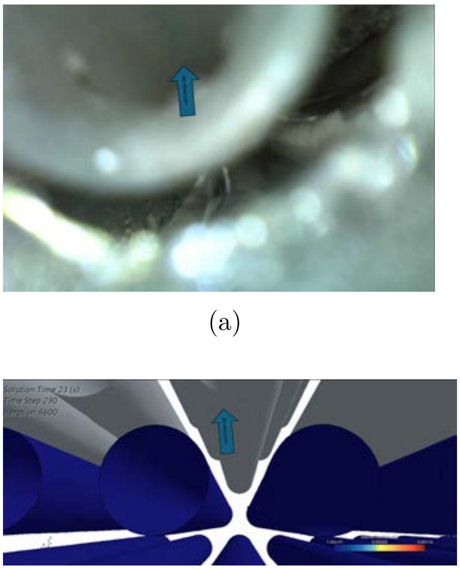

(a)

(b)

Fig. 46. (a) Experiment, (b) CFD, at ≈470 seconds into the experiment from camera 2 (see 11).

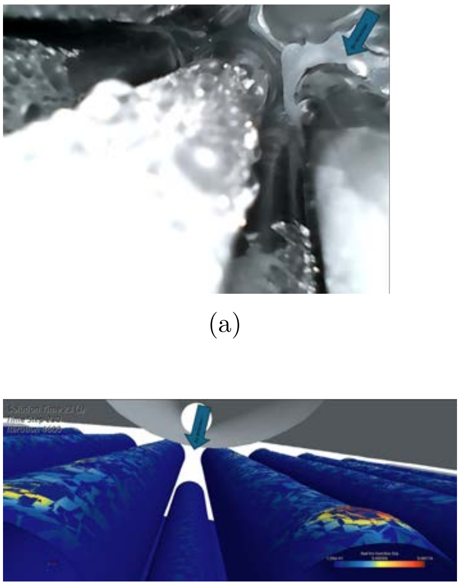

(a)

(b)

Fig. 47. (a) Experiment, (b) CFD, at ≈470 seconds into the experiment from camera 3 (see 11).

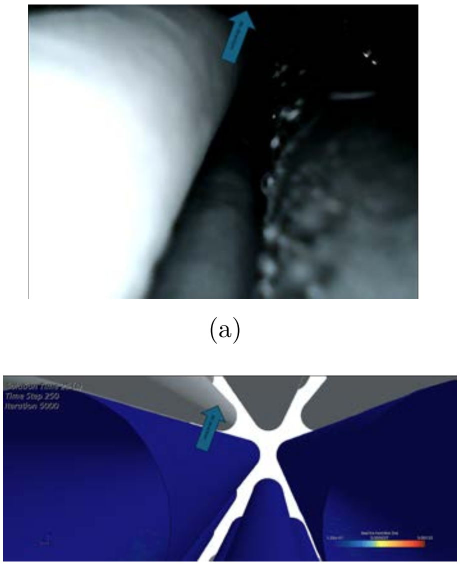

(a)

(b)

Fig. 48. (a) Experiment, (b) CFD, at ≈507 seconds into the experiment from camera 1 (see 11).

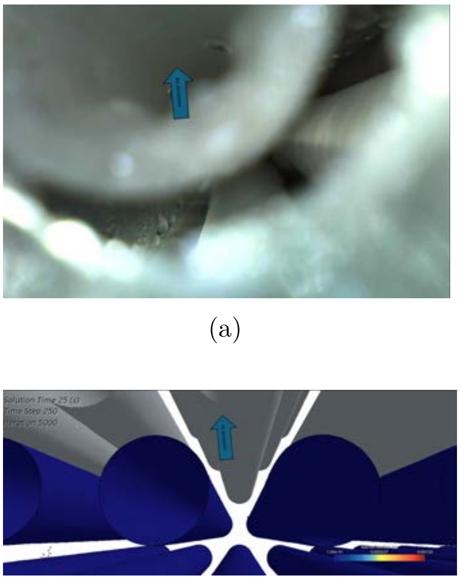

(a)

(b)

Fig. 49. (a) Experiment, (b) CFD, at ≈470 seconds into the experiment from camera 2 (see 11).

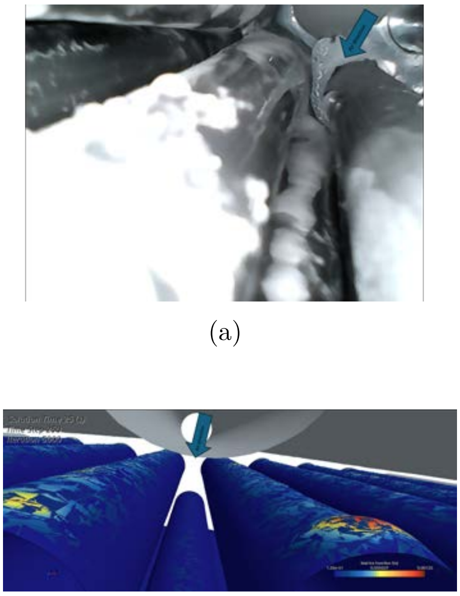

(a)

(b)

Fig. 50. (a) Experiment, (b) CFD, at ≈507 seconds into the experiment from camera 3 (see 11).

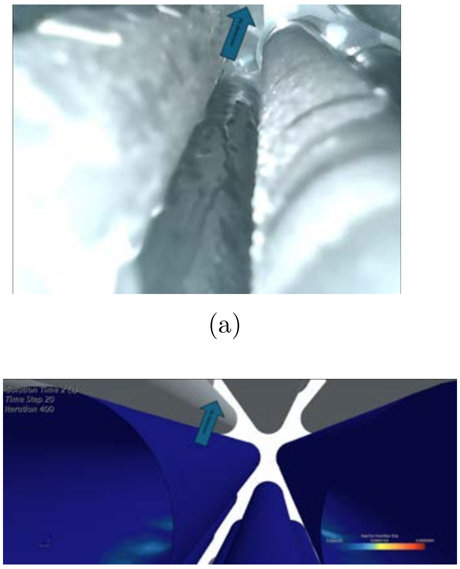

(a)

(b)

Fig. 51. (a) Experiment, (b) CFD, at ≈20 seconds into the experiment from camera 1 (see 11).

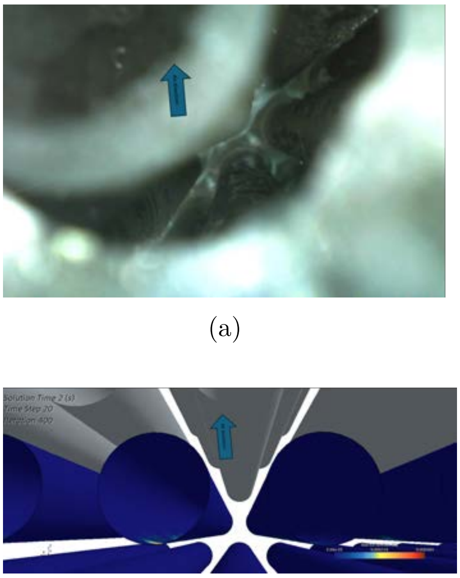

(a)

(b)

Fig. 52. (a) Experiment, (b) CFD, at ≈20 seconds into the experiment from camera 2 (see 11).

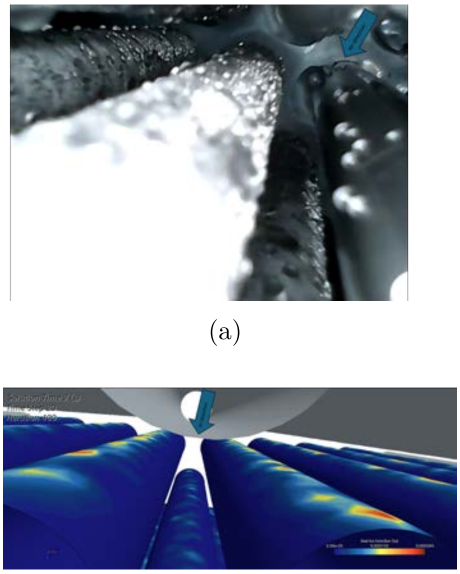

(a)

(b)

Fig. 53. (a) Experiment, (b) CFD, at ≈20 seconds into the experiment from camera 3 (see 11).

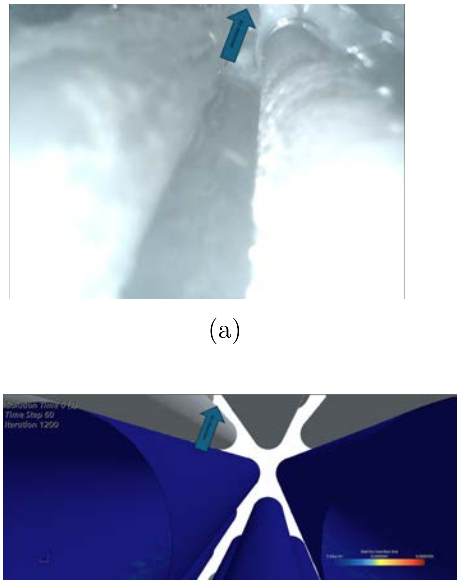

(a)

(b)

Fig. 54. (a) Experiment, (b) CFD, at ≈ 130 seconds into the experiment from camera 1 (see 11).

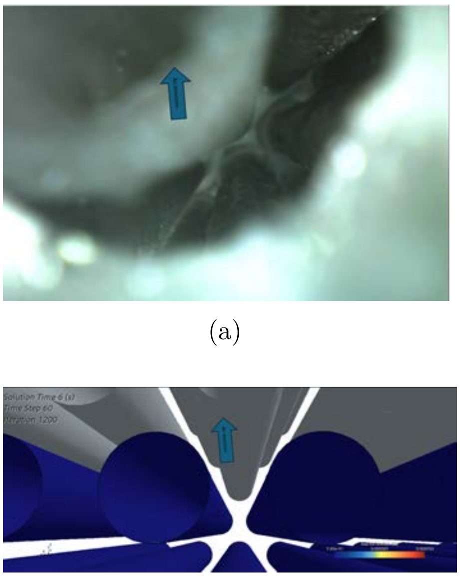

(a)

(b)

Fig. 55. (a) Experiment, (b) CFD, at ≈130 seconds into the experiment from camera 2 (see 11).

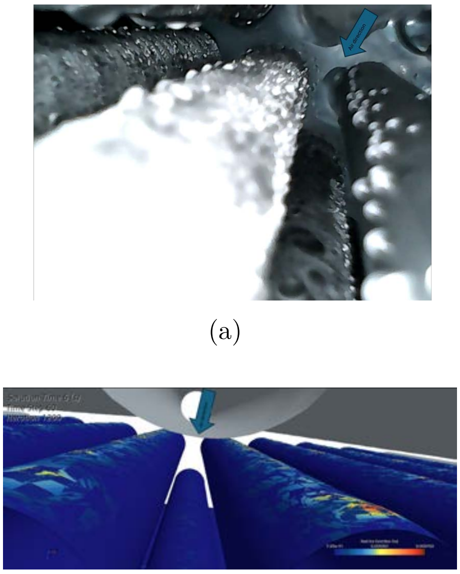

(a)

(b)

Fig. 56. (a) Experiment, (b) CFD, at ≈130 seconds into the experiment from camera 3 (see 11).

G

Error analysis code

Below the error analysis function can be seen.

```python

#!/usr/bin/env python3
# -*- coding: utf-8 -*-
"""
Created on Tue Nov 17 17:18:06 2020

Taylor Expansion tool based on Isak Jonssons .m file

@author: sudharsanvasudevan


"""
import numpy as np
import sympy as sp
import pandas as pd


def Taylor_error_propagation(Phi,dict_variables_input):

    df_variables_input = pd.DataFrame(dict_variables_input,columns=['Variables',\
                                     'Values','Error_type','Error'])

    variables = df_variables_input['Variables'].values.tolist() # list contains variable names
    values = df_variables_input['Values'].values.tolist() # list contains variable values
    Error_type = df_variables_input['Error_type'].values.tolist() # list contains type of error, absolute or percentage
    Error=df_variables_input['Error'].values.tolist() # list contains the error in estimation of each variable

    derivative_individual = []


    #computing derivative of the expression Phi with respect to each of the variables
    for var in variables:
        derivative_individual.append(sp.diff(Phi,var))
    uncertainties_individual = []

```

```
    #computing the uncertainties in estimation of the desired quantity (LHS of Phi) due to error in each of the individual variables
    for var1 in range(len(derivative_individual)):
        uncertainties_individual.append(derivative_individual[var1])
        for var2 in range(len(variables)):
            uncertainties_individual[var1]=uncertainties_individual[var1].subs(variables[var2],values[var2])
        if Error_type[var1]=='abs':
            uncertainties_individual[var1]*=Error[var1]
            #print(var1,uncertainties_individual[var1])
        else:
            uncertainties_individual[var1]*=values[var1]*0.01*Error[var1]
            # print(values[var1],Error[var1])
            #print(var1,uncertainties_individual[var1])
        uncertainties_individual[var1]=np.abs(uncertainties_individual[var1])

    #computing the square root of square of sum of individual uncertainties to obtain the final uncertatinty in the desired quantity
    sum_uncertainty = (np.sum((np.array(uncertainties_individual))**2))**0.5

    #giving a variable name for the errors (the name of the variables prefixed with 'd')
    variable_names_error=[]
    for var3 in variables:
        variable_names_error.append(sp.Symbol('( \delta '+str(var3)+' )'))

    #Final symbolic expression for total uncertainty
    Expr_uncert = (variable_names_error[0]*derivative_individual[0])**2
    for var4 in range(1,len(variables)):
        Expr_uncert += (variable_names_error[var4]*derivative_individual[var4])**2

    Expr_uncert = sp.sqrt(Expr_uncert)

    return uncertainties_individual,sum_uncertainty,Expr_uncert
```

Listing G.1: Python Taylor error function

The code that processes the error can be seen below in an example of one error source:

```

#!/usr/bin/env python3
# -*- coding: utf-8 -*-
"""

Simple tool the evaluate the accuracy of an measurment

"""
```

```python
# %% Import packages
import numpy as np
from sympy import symbols,Symbol
from Taylor_error import Taylor_error_propagation
import plotly.graph_objects as go

T = Symbol('T')
rho = Symbol('rho')
n = Symbol('n')
d = Symbol('d')

# FOr U air
h_air_int = Symbol('h_air_int')
#CT_Expr =  T / (rho * n**2 * d**4)
U_air_exp = 1/(1/(h_air_int))
dict_variables_input_q ={'Variables': [h_air_int],
                 'Values': [315.9107061],
                 'Error_type': ['abs'],
                 'Error': [50]
                 }

uncertainties_Uair,sum_uncert_Uair,Expr_uncert_Uair =
    Taylor_error_propagation(U_air_exp,dict_variables_input_q)

#CT_Expr = 3/(1.2 * (8000/60)**2 * (10*25.4e-3)**4)
U_air_exp = 1/(1/(315.9107061))


print(uncertainties_Uair)
print(sum_uncert_Uair)
print(np.divide(uncertainties_Uair,sum_uncert_Uair))
print(sum_uncert_Uair/U_air_exp)
```

Listing G.2: Python Taylor error function

H

Gannt-scheme for project

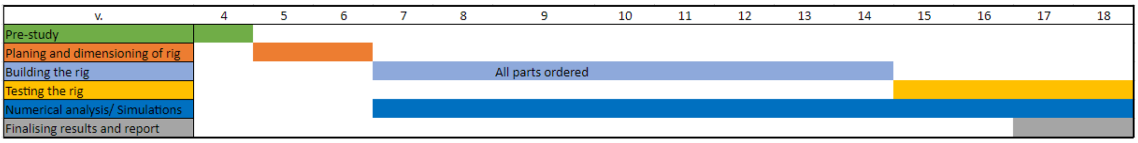

v.	4	5	6	7	8	9	10	11	12	13	14	15	16	17	18
Pre-study	🟩														
Planing and dimensioning of rig		🟧	🟧												
Building the rig				🟦	🟦	All parts ordered	🟦	🟦	🟦	🟦	🟦				
Testing the rig												🟨	🟨	🟨	🟨
Numerical analysis/ Simulations				🟦	🟦	🟦	🟦	🟦	🟦	🟦	🟦	🟦	🟦	🟦	🟦
Finalising results and report														▨	▨

Fig. 57. First generic layout of the project.

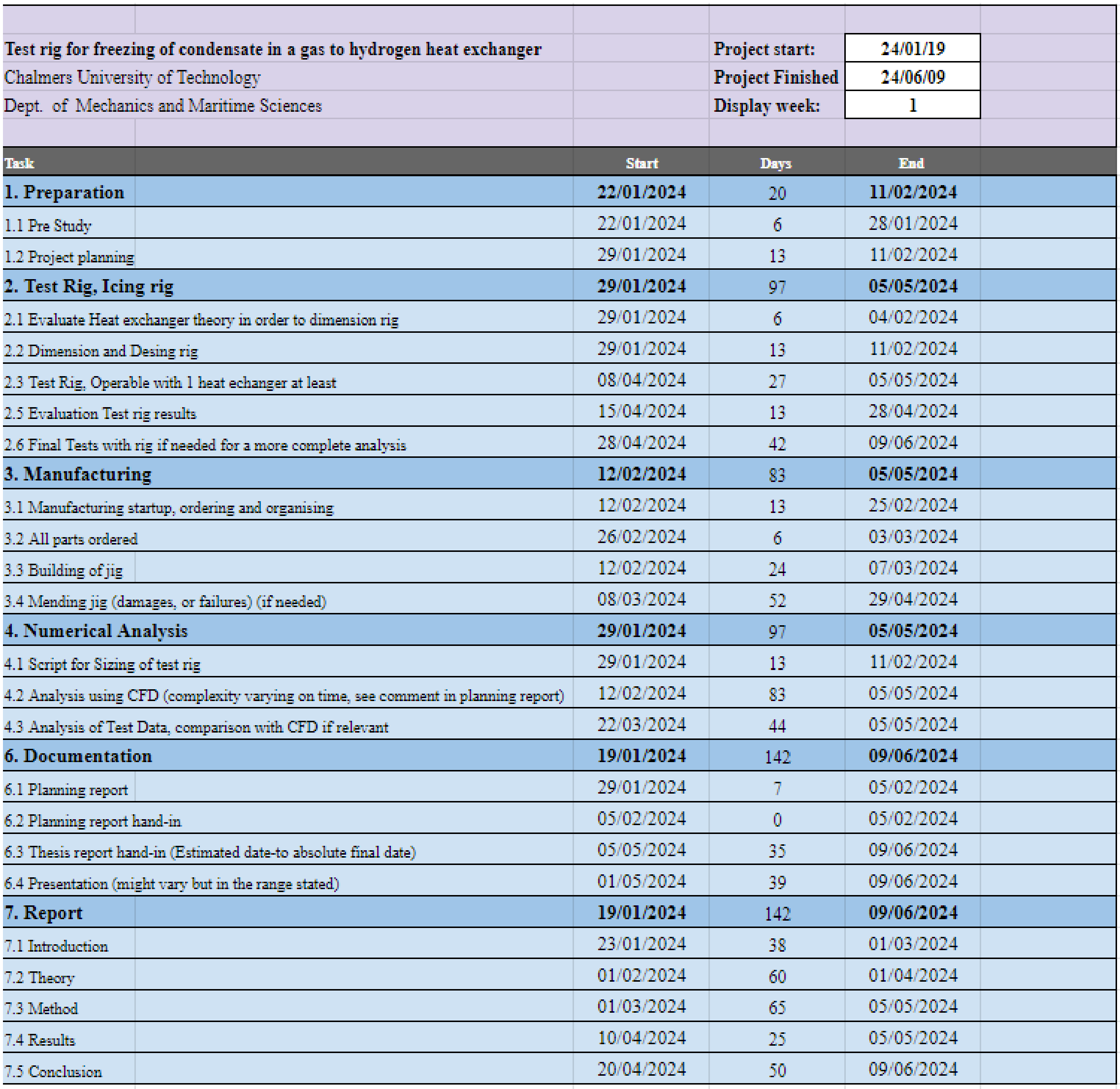

Test rig for freezing of condensate in a gas to hydrogen heat exchanger	**Project start:**	**24/01/19**	
Chalmers University of Technology	**Project Finished**	**24/06/09**	
Dept. of Mechanics and Maritime Sciences	**Display week:**	**1**	

Task	**Start**	**Days**	**End**
1. Preparation	**22/01/2024**	20	**11/02/2024**
1.1 Pre Study	22/01/2024	6	28/01/2024
1.2 Project planning	29/01/2024	13	11/02/2024
2. Test Rig, Icing rig	**29/01/2024**	97	**05/05/2024**
2.1 Evaluate Heat exchanger theory in order to dimension rig	29/01/2024	6	04/02/2024
2.2 Dimension and Desing rig	29/01/2024	13	11/02/2024
2.3 Test Rig, Operable with 1 heat echanger at least	08/04/2024	27	05/05/2024
2.5 Evaluation Test rig results	15/04/2024	13	28/04/2024
2.6 Final Tests with rig if needed for a more complete analysis	28/04/2024	42	09/06/2024
3. Manufacturing	**12/02/2024**	83	**05/05/2024**
3.1 Manufacturing startup, ordering and organising	12/02/2024	13	25/02/2024
3.2 All parts ordered	26/02/2024	6	03/03/2024
3.3 Building of jig	12/02/2024	24	07/03/2024
3.4 Mending jig (damages, or failures) (if needed)	08/03/2024	52	29/04/2024
4. Numerical Analysis	**29/01/2024**	97	**05/05/2024**
4.1 Script for Sizing of test rig	29/01/2024	13	11/02/2024
4.2 Analysis using CFD (complexity varying on time, see comment in planning report)	12/02/2024	83	05/05/2024
4.3 Analysis of Test Data, comparison with CFD if relevant	22/03/2024	44	05/05/2024
6. Documentation	**19/01/2024**	142	**09/06/2024**
6.1 Planning report	29/01/2024	7	05/02/2024
6.2 Planning report hand-in	05/02/2024	0	05/02/2024
6.3 Thesis report hand-in (Estimated date-to absolute final date)	05/05/2024	35	09/06/2024
6.4 Presentation (might vary but in the range stated)	01/05/2024	39	09/06/2024
7. Report	**19/01/2024**	142	**09/06/2024**
7.1 Introduction	23/01/2024	38	01/03/2024
7.2 Theory	01/02/2024	60	01/04/2024
7.3 Method	01/03/2024	65	05/05/2024
7.4 Results	10/04/2024	25	05/05/2024
7.5 Conclusion	20/04/2024	50	09/06/2024

Fig. 58. Detailed breakdown of milestones to acomplish in the project.

I

Error breakdown

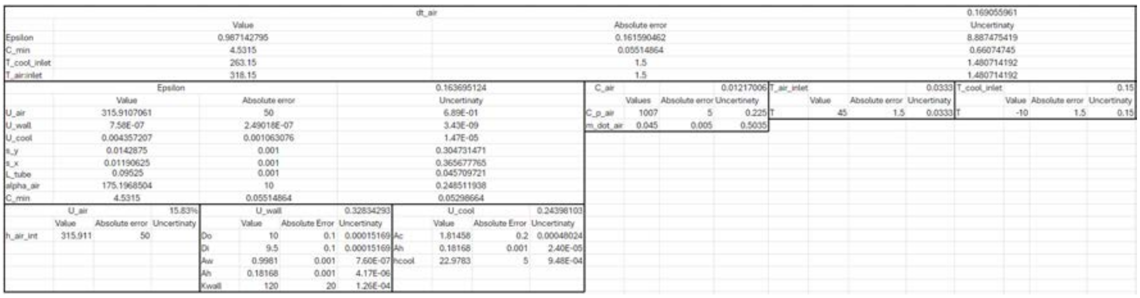

dt_air			0.169055961
	Value	Absolute error	Uncertinaty
Epsilon	0.987142795	0.161590462	8.887475419
C_min	4.5315	0.05514864	0.66074745
T_cool_inlet	263.15	1.5	1.480714192
T_air:inlet	318.15	1.5	1.480714192

Epsilon			0.163695124
	Value	Absolute error	Uncertinaty
U_air	315.9107061	50	6.89E-01
U_wall	7.58E-07	2.49018E-07	3.43E-09
U_cool	0.004357207	0.001063076	1.47E-05
s_y	0.0142875	0.001	0.304731471
s_x	0.01190625	0.001	0.365677765
L_tube	0.09525	0.001	0.045709721
alpha_air	175.1968504	10	0.248511938
C_min	4.5315	0.05514864	0.05298664

C_air			0.01217006
	Values	Absolute error	Uncertinety
C_p_air	1007	5	0.225
m_dot_air	0.045	0.005	0.5035

T_air_inlet			0.0333
	Value	Absolute error	Uncertinaty
T	45	1.5	0.0333

T_cool_inlet			0.15
	Value	Absolute error	Uncertinaty
T	-10	1.5	0.15

U_air			15.83%
	Value	Absolute error	Uncertinaty
h_air_int	315.911	50	

U_wall			0.32834293
	Value	Absolute Error	Uncertinaty
Do	10	0.1	0.00015169
Di	9.5	0.1	0.00015169
Aw	0.9981	0.001	7.60E-07
Ah	0.18168	0.001	4.17E-06
Kwall	120	20	1.26E-04

U_cool			0.24398103
	Value	Absolute Error	Uncertinaty
Ac	1.81458	0.2	0.00048024
Ah	0.18168	0.001	2.40E-05
hcool	22.9783	5	9.48E-04

Fig. 59. Image of the entire error breakdown in the first case.

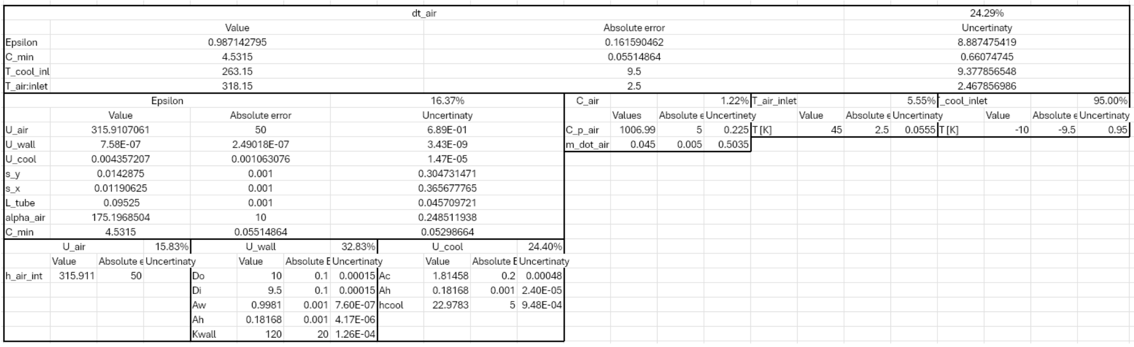

dt_air			24.29%
	Value	Absolute error	Uncertinaty
Epsilon	0.987142795	0.161590462	8.887475419
C_min	4.5315	0.05514864	0.66074745
T_cool_inl	263.15	9.5	9.377856548
T_air:inlet	318.15	2.5	2.467856986

Epsilon			16.37%
	Value	Absolute error	Uncertinaty
U_air	315.9107061	50	6.89E-01
U_wall	7.58E-07	2.49018E-07	3.43E-09
U_cool	0.004357207	0.001063076	1.47E-05
s_y	0.0142875	0.001	0.304731471
s_x	0.01190625	0.001	0.365677765
L_tube	0.09525	0.001	0.045709721
alpha_air	175.1968504	10	0.248511938
C_min	4.5315	0.05514864	0.05298664

C_air			1.22%
	Values	Absolute e	Uncertinety
C_p_air	1006.99	5	0.225
m_dot_air	0.045	0.005	0.5035

T_air_inlet			5.55%
	Value	Absolute e	Uncertinaty
T [K]	45	2.5	0.0555

_cool_inlet			95.00%
	Value	Absolute e	Uncertinaty
T [K]	-10	-9.5	0.95

U_air			15.83%
	Value	Absolute e	Uncertinaty
h_air_int	315.911	50	

U_wall			32.83%
	Value	Absolute E	Uncertinaty
Do	10	0.1	0.00015
Di	9.5	0.1	0.00015
Aw	0.9981	0.001	7.60E-07
Ah	0.18168	0.001	4.17E-06
Kwall	120	20	1.26E-04

U_cool			24.40%
	Value	Absolute E	Uncertinaty
Ac	1.81458	0.2	0.00048
Ah	0.18168	0.001	2.40E-05
hcool	22.9783	5	9.48E-04

Fig. 60. Image of the entire error breakdown in the second case.